sustainability

Article

# Economic Viability of NaS Batteries for Optimal Microgrid Operation and Hosting Capacity Enhancement under Uncertain Conditions

**Mohammed M. Alhaider [1,*], Ziad M. Ali [1,2,*], Mostafa H. Mostafa [3] and Shady H. E. Abdel Aleem [4]**

[1] Department of Electrical Engineering, College of Engineering in Wadi Alddawasir, Prince Sattam Bin Abdulaziz University, Wadi Alddawasir 11991, Saudi Arabia
[2] Electrical Engineering Department, Aswan Faculty of Engineering, Aswan University, Aswan 81542, Egypt
[3] Electrical Power and Machines Department, International Academy for Engineering and Media Science, Cairo 12411, Egypt; m.h.mostafa2050@gmail.com
[4] Department of Electrical Engineering, Institute of Aviation Engineering and Technology, Giza 12658, Egypt; shady.abdelaleem@iaet.edu.eg
* Correspondence: m.alhaider@psau.edu.sa (M.M.A.); dr.ziad.elhalwany@aswu.edu.eg (Z.M.A.)

**Abstract:** Recent developments have increased the availability and prevalence of renewable energy sources (RESs) in grid-connected microgrids (MGs). As a result, the operation of an MG with numerous RESs has received considerable attention during the past few years. However, the variability and unpredictability of RESs have a substantial adverse effect on the accuracy of MG energy management. In order to obtain accurate outcomes, the analysis of the MG operation must consider the uncertainty parameters of RESs, market pricing, and electrical loads. As a result, our study has focused on load demand variations, intermittent RESs, and market price volatility. In this regard, energy storage is the most crucial facility to strengthen the MG's reliability, especially in light of the rising generation of RESs. This work provides a two-stage optimization method for creating grid-connected MG operations. The optimal size and location of the energy storage are first provided to support the hosting capacity (HC) and the self-consumption rate (SCR) of the RESs. Second, an optimal constrained operating strategy for the grid-connected MG is proposed to minimize the MG operating cost while taking into account the optimal size and location of the energy storage that was formerly determined. The charge–discharge balance is the primary criterion in determining the most effective operating plan, which also considers the RES and MG limitations on operation. The well-known Harris hawks optimizer (HHO) is used to solve the optimization problem. The results showed that the proper positioning of the battery energy storage enhances the MG's performance, supports the RESs' SCR (reached 100% throughout the day), and increases the HC of RESs (rising from 8.863 MW to 10.213 MW). Additionally, when a battery energy storage system is connected to the MG, the operating costs are significantly reduced, with a savings percentage rate of 23.8%.

**Keywords:** economic analysis; hosting capacity; market price; microgrid; bi-level optimization; renewable energy sources; sodium–sulfur batteries; uncertainty



**Citation:** Alhaider, M.M.; Ali, Z.M.; Mostafa, M.H.; Aleem, S.H.E.A. Economic Viability of NaS Batteries for Optimal Microgrid Operation and Hosting Capacity Enhancement under Uncertain Conditions. *Sustainability* **2023**, *15*, 15133. https://doi.org/10.3390/su152015133

Academic Editor: George Kyriakarakos

Received: 14 September 2023
Revised: 16 October 2023
Accepted: 20 October 2023
Published: 22 October 2023



## 1. Introduction

Due to the rapid growth of the international economy, electricity demand is increasing dramatically. As a result, pollution of the environment and fuel shortage are ongoing issues [1]. The global electricity market report demonstrates the strong connection between the growth of the global economy and the increase in electricity demand. In 2021, the worldwide gross domestic product increased by 5.9%, while in 2022, it increased by 4.9%. As a result, the global electricity demand increased by 6% in 2021 and 2.4% in 2022 [2]. To meet electrical requirements and reduce pollution, renewable energy sources (RESs) are used [3,4]. Nearly 320 GW of RES capacity was available in 2022: an increase of over 8%.

On the other hand, excessive usage of RESs may result in issues with the power system [5], including overloaded electrical system components, increased power losses, increased transmission line loading, issues with over-voltage, and a higher risk of short circuits [6,7].

Diverse techniques are used in research studies to address these issues and boost the capacity of RESs:

- The conventional grid support technique employs a variety of economically effective autonomous inverter control techniques [8].
- To reserve bus voltage in this manner, a tap changer with a low-voltage transformer is utilized [9].
- Active power curtailment of RESs approach that uses active power curtailment schemes to avoid voltage increases in feeders with high RES penetration [10].
- Demand-side management method: with this approach, users' energy consumption is decreased to diminish the issue of overvoltage [11].
- Reactive power control method: in this method, the relationship between the reactive power and active power of RESs is controlled to support the voltage buses of the electrical system [12].
- Energy storage systems (ESSs) address the issues brought on by high RES generation; the ESS is incorporated into the electrical power system in this approach [13].

In order to support renewable energies, the RES's hosting capacity (HC) without electrical operational issues must be improved [14]. The microgrid (MG) aims to combine RESs for self-consumption, using the energy as it is being produced to make RESs a commoditized alternative for electricity production and more cost-effective [15]. Therefore, RES generation is prioritized for self-consumption. In order to reduce overall operating costs, excess RES output should be added to the distribution or transmission grid when RES power exceeds the electrical load, i.e., to be stored [16–19].

Bearing these considerations in mind, enhancing the HC of RESs becomes crucial for the MGs and electrical power systems in general. Additionally, many factors, including topographical boundaries and intermittency, adversely impact the output power of RESs; managing these factors presents a significant problem [19,20]. A promising piece of equipment is an ESS, which has the potential to increase system reliability, increase its capacity for renewable energy sources, and make it more resilient to interruptions [21].

In order to improve the performance of electrical power systems, such as lowered transmission losses, increased energy efficiency, supported power quality, and reduced environmental pollution [22], MG systems connect ESS units, renewable and non-renewable energy resources, and diverse controllers. In addition, the transformer connecting the main grid and the MG can occasionally experience an overload because of the increased electrical load [23]. The accepted approach thus calls for strengthening the transformer to boost its capacity (reinforcement), but drawbacks include a lack of ability to reinforce the transformer and a low rate of return on investment [24]. As a result, to address the issue of transformer overloading, demand during peak hours must be reduced [25]. As a result, the method used to implement the best ESS allocation and reasonably schedule the output power of distributed generators (DGs), ESSs, and main grids in accordance with conditions for renewable and non-renewable energy resources and electrical demand not only affects the consistency of the energy supply of the electrical power system but also controls the cost and reliability of its operation to a significant extent.

The battery management system (BMS) is essential for controlling the state of power batteries, ensuring their safety, and improving their service efficiency [26]. BMS should keep the battery in appropriate working conditions and protect it from overcharge, over-discharge, and abnormal thermal conditions. A battery is a multistate, complicated nonlinear system. As a result, creating an effective and precise BMS serves as both the foundation for battery control and the key to successful battery management [27]. Battery data gathering, modeling and state estimation, charge and discharge control, problem detection and warning, temperature management, balancing control, and communication are only a few of a BMS's fundamental duties, as depicted in Figure 1 [28]. SOX algorithms improve

BMS and increase battery health and performance by measuring and predicting the state of energy, state of charge, state of power, and state of health of the battery with a high degree of accuracy, better fault tolerance, and robustness [29]. BMS controls the temperature of batteries to keep them working safely and effectively. Low temperatures can cause a reduction in battery capacity and poorer charging/discharging efficiency, while high temperatures can hasten battery aging and pose safety issues [30]. After each charging cycle, the voltages of all the cells in the battery pack are equalized through a process called battery balancing. Either the highest-charged cell is discharged, or the charge is transferred from one cell to another cell. Thus, the equalization management systems, one of the major components of the BMS, are essential to reducing such inter-cell inconsistency by redistributing the energy among the cells [31]. Due to the growing use of batteries in highly complex and powerful applications, fault detection has emerged as a critical function of the BMS. This is performed to guarantee the system's safe and dependable functioning [32].

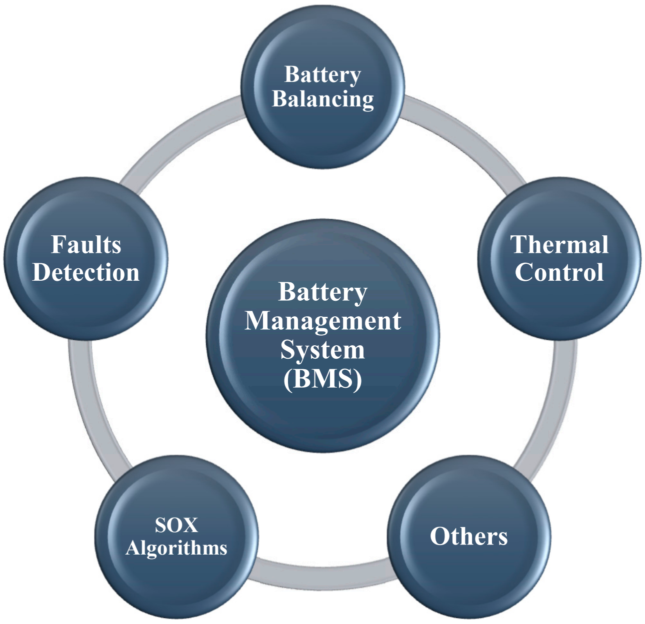


**Figure 1.** Main functions of a battery management system.

BMS is not the same for all types of batteries or schemes. It is designed specifically for the type of battery it is meant to manage. Different batteries have different chemistries, voltages, and charge/discharge characteristics, so the BMS needs to be tailored to these specifics [33]. For example, lithium-ion batteries require a different BMS compared to lead–acid batteries. The BMS for a lithium-ion battery needs to monitor factors such as cell voltage, temperature, and state of charge to ensure safe and efficient operation. Lead–acid batteries have different parameters that need to be monitored [34]. Additionally, different schemes (such as series or parallel configurations) may require specialized BMS setups to ensure that each cell or battery module is properly balanced and protected. It is crucial to match the BMS with the specific battery chemistry and configuration to optimize performance and safety [35]. The BMS for sodium–sulfur (NaS) batteries is unique to this specific type of battery chemistry. NaS batteries operate on a high-temperature principle, utilizing molten sodium and sulfur as active materials [36]. The BMS for NaS batteries needs to be designed to handle the unique characteristics of this chemistry. It monitors parameters such as temperature, cell voltage, state of charge, and cell balancing. Additionally, it manages the high operating temperatures that NaS batteries require for proper function. Since NaS batteries are commonly used in large-scale energy storage applications, the BMS also plays a critical role in ensuring the safety, performance, and longevity of the battery system. It helps prevent issues such as overcharging, over-discharging, and thermal runaway, which are crucial for maintaining the integrity of the battery and preventing safety hazards. The BMS for NaS batteries is tailored to the specific characteristics and operating conditions of NaS chemistry, ensuring the safe and efficient operation of these high-temperature batteries [37].

In order to improve the operation of the MG, various research papers have been published in recent years to examine the best ESS allocation and schedule the output power of DGs, ESSs, and the main grid. Numerous articles focused solely on the optimal ESS size [38–40]. For instance, active dispatch mode, a novel method suggested by Li et al. [38], allows for optimizing ESS capacity while enhancing electrical power system reliability. Additionally, the developed method considered the uncertainty characteristics and operated the ESS to shift peak demand. To reduce the cost of maintaining the electrical power system, Hou et al. [39] developed an optimal capacity model for wind turbines, photovoltaics, and ESSs. The model considered various ESS kinds, including compressed air, gravity storage, and battery storage. A mixed-integer linear program was suggested by Panuschka and Hofmann [40] to optimize the ESS in large industrial loads and increase flexibility. Additionally, many studies [41–43] focus on investigating how the ESS's location affects the functionality of the MG in addition to its size. In order to reduce the cost of operating the MG, Chen and Duan [41] presented an optimization methodology for determining the best location and size for ESS and DG. Mostafa et al. [42] presented an optimization technique to obtain the best ESS allocation for improving the voltage stability and performance of the MG by lowering power losses. A mathematical model was developed by Qiu et al. [43] to analyze the best ESS and micro-turbine scheduling and energy scheduling for the MG to manage its operation. However, most of the earlier studies had not looked at the effects of ESSs on the SCR, HC of the RESs, and overloading rates of transformers.

This work addresses this research gap by introducing a two-stage optimization approach to develop the operation of grid-connected MG while taking market price volatility, intermittent RES, and fluctuations in electricity demand into account. Firstly, the optimal size and location of the ESS are determined to support the HC and the SCR rate of the RESs. Secondly, the optimal working strategy is executed for the grid-connected MG to minimize the MG working cost, considering the EES's optimal size and location, which was obtained first.

The explained problem is investigated using the Harris hawks optimizer (HHO). During its wildlife rabbit hunting operations, the HHO imitates Harris hawks. With this intelligent strategy, Harris hawks can imitate several hunting attitudes based on different situations and rabbit evasion techniques [44]. HHO is superior to several swarm intelligence optimization algorithms, including Gaussian process optimization, firefly algorithm, biogeography-based optimization, particle swarm optimization, and grey wolf optimization algorithm, according to results verified over a variety of engineering optimization problems and benchmark functions [44]. The outcomes also show that HHO achieves a respectable balance between exploitation and exploration, enhancing the HHO's capacity to produce superior outcomes [44]. Furthermore, [45] demonstrated that the HHO is a potentially significant optimizer that supports the investigation of complex non-linear problems.

The following is a summary of this paper's principal advances:

- This work examines the impact of the ESS on RES hosting capacity and transformer loads connected to the MG with the main grid.
- An optimal ESS allocation is proposed to support the self-consumption rate of the RESs and reduce the overall operating costs of the MG while taking into account the actual operation of the MG with a high penetration level of RESs and taking market price volatility, intermittent RES, and changes in electrical load demand into account.
- The presented operation mode operates ESS units actively to optimally utilize the benefits from the ESS and minimize the operation cost of the various DGs included in the MG, taking into account the various cost factors, efficiency, and lifecycle of ESS. This is performed through operation constraints of the grid-connected MG, real-time modification, and energy management strategies.

The rest of the article is structured as follows: The MG arrangement, HC for RESs, and modeling of uncertainty are clarified in Section 2. The problem's mathematical formulation, HHO, and its application to address the problem are presented in Section 3. In Section 4, we give the simulation findings and discuss them. Section 5 concludes with a brief review of the work completed, the findings of the study, and future research.

## 2. Microgrid Configuration

The IEEE 33-bus system discussed in [13] has been employed in this study. The MG under-investigation is depicted in Figure 2. The entire data from [13] for each photovoltaic (PV) and wind turbine (WT) unit is provided in Table 1.

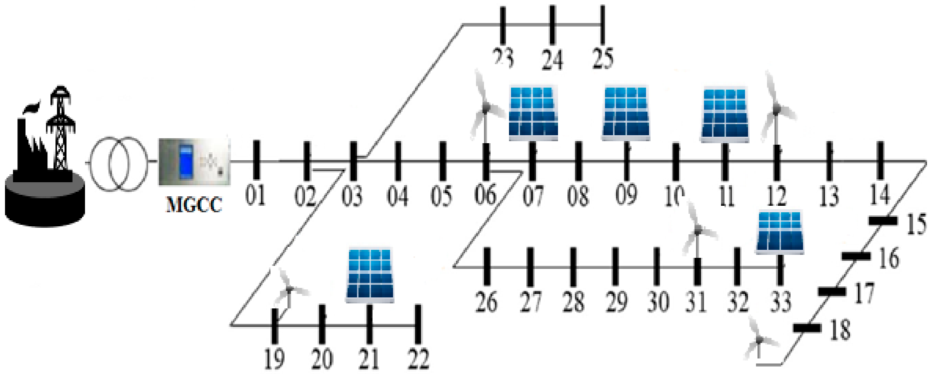


**Figure 2.** The MG investigated in this study.

**Table 1.** The entire data for WTs and PVs.

| RES Type | Properties | Values | | | | |
|---|---|---|---|---|---|---|
| PV | Location | 7 | 9 | 11 | 21 | 33 |
| | size (MW) | 0.24 | 0.36 | 0.36 | 0.36 | 0.6 |
| WT | Location | 6 | 12 | 18 | 19 | 31 |
| | size (MW) | 1.2 | 0.6 | 0.6 | 0.96 | 1.2 |

### 2.1. Wind Turbine Units

The WT units related to wind speed are usually separated into four parts, as expressed in Equation (1) [19].

$$Power_h^{WT} = \begin{cases} 0 & vel_{WT,h} < vel_{WT}^{cut-in} \\ Power_R^{WT}\left(\frac{(vel_{WT,h})^3-(vel_{WT}^{cut-in})^3}{(vel_{RWT})^3-(vel_{WT}^{cut-in})^3}\right) & vel_{WT}^{cut-in} \le vel_{WT,h} < vel_{RWT} \\ Power_R^{WT} & vel_{RWT} \le vel_{WT,h} < vel_{WT}^{cut-out} \\ 0 & vel_{WT,h} \ge vel_{WT}^{cut-out} \end{cases} \quad (1)$$

where $vel_{WT,h}$, $vel_{RWT}$, $vel_{WT}^{cut-out}$, and $vel_{WT}^{cut-in}$ express the current hourly wind speed, rated WT speed, the cut-out WT speed, and cut-in WT speed, respectively. $Power_h^{WT}$ and $Power_R^{WT}$ denote the output and rated powers of the WT, respectively.

### 2.2. Photovoltaic (PV) Stations

The output power of a PV station relates to the solar irradiance and the ambient temperature, as represented by Equation (2) [19].

$$Power_h^{PV} = NU^{PV} Power_R^{PV}\left(\frac{GI}{GI_0}\right)\left(1 - TC_{coff}(TC_{ambient} - 25)\right)\eta_v \eta_R \quad (2)$$

where $Power_R^{PV}$ and $Power_h^{PV}$ express the rated power and the output of the PV stations. $\eta_v$ and $\eta_R$ express the efficiency of the inverter and the PV relative efficiency. $NU^{PV}$ denotes the number of PV stations. $TC_{coff}$ and $TC_{ambient}$ express the temperature coefficient and the ambient temperature. $GI$ and $GI_0$ are the global and standard solar irradiance under standard test conditions.

### 2.3. Operation of the Main Grid

The operation cost of the main grid $\left(Cost^{grid}\right)$ relates to the output of the main grid $\left(Power_h^{grid}\right)$ and market energy price $\left(MP_h^{grid}\right)$ in (USD/kW) considering several market price scenarios $(NS)$ and their probabilities $\left(x_h^s\right)$ as represented by Equation (3).

$$Cost^{grid} = \sum_{s=1}^{NS}\left(x_h^s.MP_h^{grid}\cdot Power_h^{grid}\right) \tag{3}$$

### 2.4. Battery Storage System

Battery energy storage systems (BSSs) come in a variety of forms, including lead–acid, lithium-ion, sodium–sulfur, nickel–cadmium, etc. [21]. The HC value of RES, grid stability, power calculations, peak load reduction, and energy management of the MG are all obviously impacted differently by each type's technological characteristics [19]. The technology of NaS is one of the most promising ones, which uses liquid sodium as the negative electrode and liquid sulfur as the positive electrode and is composed of inexpensive materials. High energy capacity, high efficiency, long cycling life, high operating temperature, and reasonable prices are some of the benefits of NaS batteries [5,15]. Additionally, Mostafa et al. [21] developed a methodology for calculating storage costs that considers both the technical and economic aspects of each storage type's many storage types. The conclusion of the study confirmed that because of its high efficiency, long lifespan, and affordable replacement prices, NaS storage offers the best cost among alternative storage options.

The capital cost ($BSS_c$) of the BSS is related to its power ($Power^{BS}$) and energy ($Energy^{BS}$) capacities as given in Equation (4).

$$BSS_c = \left(Cost^P\cdot Power^{BS}\right) + \left(Cost^E\cdot Energy^{BS}\right) \tag{4}$$

where $Cost^P$ (USD/kW) and $Cost^E$ (USD/kWh) are the costs related to the power and energy sizes of the storage.

### 2.5. Renewable Energy Hosting Capacity

The electrical power system used to be one-way, with energy flowing from the main grid to demands. The electrical network should allow for an exchange of power as RESs are increasingly used [46]. The high penetration level of RES, however, could have an adverse impact on how the electrical power grid functions and possibly result in several operational issues, including overloading of electrical system components, increased power losses, increased transmission line loading, overvoltage issues, and an increased risk of short circuits [47]. Researchers must determine how many RESs the power grid can accommodate without surpassing its operational limit. Electrical power system RES capacity may expand despite power grid limits [48]. Supporting the electrical network's HC increases RES penetration without electrical problems [48]. Figure 3 shows RES hosting capacity. Hosting capacity of RESs ($HCRES$) represents the ratio between the injected output power of RESs ($Power_{RESs}$) and the apparent power of demand ($S_{load}$), as given in Equation (5) [47]. The self-consumption rate of RESs ($\Psi$) expresses the ratio between the actual energy of RES ($Energy_{RES}$) and the overall produced RES energy ($Energy_{RES}^{rated}$) as given in Equation (6) [48].

$$HCRES\% = \frac{Power_{RESs}}{S_{load}}\cdot 100 \tag{5}$$

$$\Psi = \frac{Energy_{RES}}{Energy_{RES}^{rated}} \tag{6}$$

The power systems need to improve $\Psi$ and *HCRES*. The ESSs are essential electrical network elements that can effectively perform this [49].

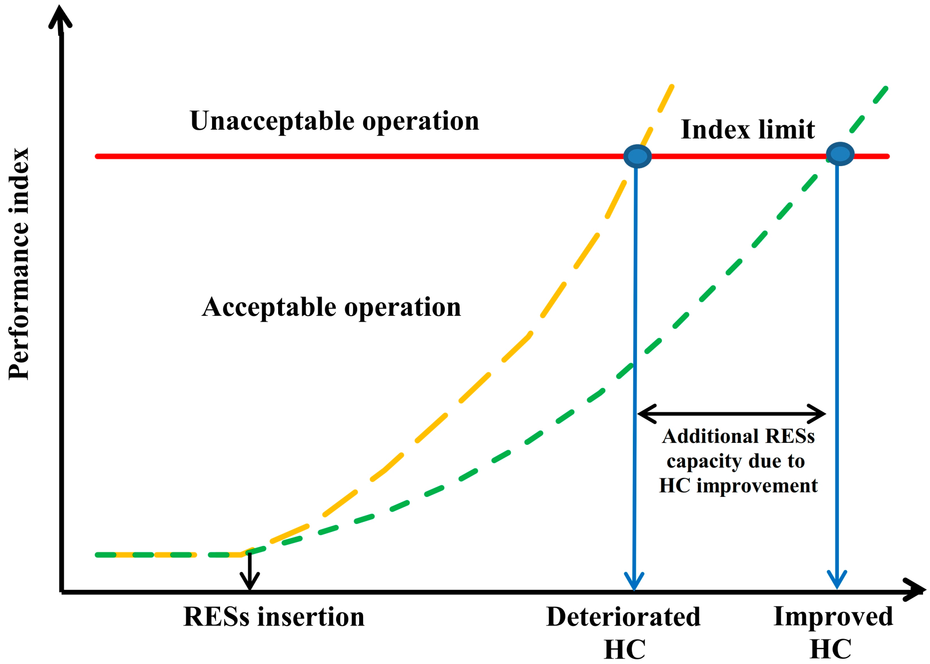


**Figure 3.** The HC and the importance of its support (as noted by the green dashed line).

*2.6. Uncertainty Modeling*

In stochastic optimization, creating suitable scenarios is crucial to enabling decisions based on precise assessments of uncertainties [19]. As a result, to accurately reflect the usual measurement, the uncertainties' estimations must use a realistic method. Each uncertainty modeling technique would require a distinct design for the system. Consequently, it is critical to use the appropriate approach when modeling uncertainty. In contrast to the deterministic technique, which relies on precise knowledge of well-known characteristics, uncertainty modeling simulates the volatility in market price, RES output power, and electrical load. In order to imitate the probability properties of the parameters, random distributions are employed as inputs to the random optimization problem [50]. To illustrate the numerous system parameter uncertainties, this study develops a number of scenarios, each with a known probability. Uncertain scenarios for electricity demand, RES capacity for generation, and market pricing are generated using the fuzzy clustering method (FCM). Then, grouping these instances into a more reasonable set is desirable.

FCM is used in this work to split a specific number of data ($M$) into a specific number of clusters ($O$), with $O$ = 10, as specified in [51]. As the number of scenarios rises, the problem becomes more complex and challenging, requiring a larger processing package.

A matrix $Z$ with a collection of column vectors $z_j$, where $j$ = 1, 2,..., $M$, collects the data required for clustering. To group $Z$, FCM requires the elements $O$ and the fuzziness component ($d$), where $d > k$ and $d > 1$. The procedure is presupposed to end at a predetermined tolerance (*eps*). There are five phases in the FCM clustering algorithm:

- Phase 1: A membership matrix ($k = [k_{ij}]_{O\times M}$) is initialized randomly, where the sum of each column $j$ in $k$ must equal 1. $O$ random centroids are chosen from the data. These centroids are gathered in a vector $= [O_i]_{1\times O}$.

- Phase 2: compute the new centroids utilizing Equation (7):

$$O_i = \frac{\sum_{i=1}^{M} k_{ij}^{d} \times z_j}{\sum_{i=1}^{M} k_{ij}^{d}} \tag{7}$$

- Phase 3: compute the elements of the membership matrix $\left(k = \left[k_{ij}\right]_{O\times M}\right)$ for each element in $Z$, where:

$$k_{ij} = \frac{1}{\sum_{p=1}^{O} \left(\frac{\|z_j - O_i\|}{\|z_j - O_p\|}\right)^{\frac{2}{d-1}}} \tag{8}$$

- Phase 4: compute $f_{FCM}^{(n)} = \sum_{j=1}^{M} \sum_{i=1}^{O} k_{ij}^{d} \|z_j - O_i\|$, where $f_{FCM}^{(n)}$ represents the objective function value at the $n$th iteration.
- Phase 5: if $\left\| f_{FCM}^{(n)} - f_{FCM}^{(n-1)} \right\| < eps,\ \forall n$, stop the algorithm; otherwise, repeat the procedure starting from Phase 2.

## 3. Problem Formulation

Problem formulation can be divided into objective function system constraints and optimization algorithms, as follows.

### 3.1. Objective Function

Two levels are used to introduce the objective function. First, the BSS's optimal size and location, as specified by $OF_1$ in Equation (9), are implemented to increase the SCR of all RESs in the MG, where $\Psi(x)$ reflects the self-consumption of all RESs in the MG. Second, using the optimal BSS size and position that was initially determined, an optimal operating strategy is implemented for the grid-connected MG, as shown in Equation (10), to reduce the MG operating cost where $OF_2$ expresses the total cost of BSS per day ($TCSS$) (USD/day), generation costs of WT and PV (USD/kWh), and the operation cost of the utility (USD/kWh), considering the several PV output power scenarios $(MS)$ and their probabilities $\left(b_h^{pv,s}\right)$, several WT output power scenarios $(WS)$ and their probabilities $\left(b_h^{wt,s}\right)$, and numerous market price scenarios $(NS)$ and their probabilities $\left(x_h^s\right)$.

$$OF_1 = \max\Psi(x) = \sum_{h=1}^{H} \left(\frac{Energy_{RES,h}}{Energy_{RES,h}^{rated}}\right) \tag{9}$$

$$OF_2 = \sum_{h=1}^{H} \sum_{s=1}^{NS} \left(x_h^s \cdot MP_h^{grid} \cdot Power_h^{grid}\right) + \sum_{s=1}^{MS} \left(b_h^{pv,s} \cdot B_h^{PV} \cdot Power_h^{PV}\right) + \sum_{s=1}^{WS} \left(b_h^{wt,s} \cdot B_h^{WT} \cdot Power_h^{WT}\right) + TCSS \tag{10}$$

where $Energy_{RES,h}$ and $Energy_{RES,h}^{rated}$ are the total RESs energy. $Power_h^{grid}$, $Power_h^{WT}$, and $Power_h^{PV}$ are the main grid, WT, and PV output powers at each hour $h$, respectively. $MP_h^{grid}$, $B_h^{WT}$, and $B_h^{PV}$ are the kWh price of the main grid, WT, and PV at $h$, respectively.

Life cycle assessment includes all costs of batteries, such as capital cost, operation and maintenance cost, and replacement cost of batteries [52]. In this research, it was assumed that the purchase price of BSS covers all of its components, including the capital and replacement costs during the course of the project. The capital cost ($CBS_c$) of the BSS is related to its power ($Power^{BS}$) and energy ($Energy^{BS}$) capacities as given in Equation (11).

$$CBS_c = \left(Cost^P \cdot Power^{BS}\right) + \left(Cost^E \cdot Energy^{BS}\right) \tag{11}$$

where $Cost^P$ (USD/kW) and $Cost^E$ (USD/kWh) are the coefficient cost of BSS function of rated power of BSS and its energy. To obtain the replacement number of BSS, first, the number of cycles achieved over the BSS $(Battery_{cycles})$ is obtained by Equations (12) and (13) to determine the BSS lifetime. Second, Equation (14) used to obtain the lifetime of BSS ($L_{BS}$) relying on the life cycle of a battery ($Battery_{Lifecycles}$) and $Battery_{cycles}$.

$$n_{Battery}(h,j) = \left(k_{a(h)} - k_{a(h-1)}\right) y_{a(h)}, \quad \forall h \in H, \forall j \in D \tag{12}$$

$$Battery_{cycles} = \sum_{j=1}^{D} \sum_{h=1}^{H} n_{Battery}(h,j) \tag{13}$$

$$L_{BS} = \frac{Battery_{Lifecycles}}{Battery_{cycles}} \tag{14}$$

where $n_{Battery}(h,j)$ expresses the BSS cycles, and $D$ represents the total number of operating days per year. BSS has two statuses: charge and discharge, $k_{a(h)}$ represents the status of BSS at each hour during the operating days per year. Therefore, the BSS replacement number ($RN_{Battery}$) through the project lifetime ($Q$) is represented by Equation (15).

$$RN_{Battery} = \frac{Q}{L_{BSS}} \tag{15}$$

Accordingly, $TCSS$ (USD/day) can be obtained by using Equation (16) as a function of the interest rate $i$.

$$TCSS = \frac{1}{D \cdot Q} \left( \frac{i(1+i)^{Q}}{(1+i)^{Q} - 1} \cdot CBS_c \cdot RN_{Battery} \right) \tag{16}$$

*3.2. Constraints*

For the solution to be applicable, the investigation must incorporate many sets of constraints, as follows:

3.2.1. RES Constraints

The generated power by WT must be restricted by its minimum power value $Power^{WT}_{h,min}$ and its maximum power value $Power^{WT}_{h,max}$ as represented in Equation (17). Similarly, the generated power by PV must be restricted by its minimum power value $Power^{PV}_{h,min}$ and its maximum power value $Power^{PV}_{h,max}$ as represented in Equation (18).

$$Power^{WT}_{h,min} \leq Power^{WT}_{h} \leq Power^{WT}_{h,max}, \forall h \tag{17}$$

$$Power^{PV}_{h,min} \leq Power^{PV}_{h} \leq Power^{PV}_{h,max}, \forall h \tag{18}$$

3.2.2. Power Balance

The total produced output power from the different DGs must be equal to the total load scenarios $(P_{load,s,h})$ and their probabilities ($\psi^{s,h}$) at all times during the day, as represented in Equation (19).

$$\begin{aligned} \sum_{s=1}^{NS} x^{s}_{h} \cdot Power^{grid}_{h} \quad & + \textstyle\sum_{s=1}^{MS} \left( b^{pv,s}_{h} \cdot Power^{PV}_{h} \right) + \textstyle\sum_{s=1}^{WS} \left( b^{wt,s}_{h} \cdot Power^{WT}_{h} \right) \\ & + Power^{BS}_{DIS,h} \\ & = \textstyle\sum_{s=1}^{LS} \left( \psi^{s,h} \cdot P_{load,s,h} \right) + Power^{BS}_{CH,h} + \sum_{b=1}^{NR} Power^{losses}_{b,h} \quad \forall h \in H \end{aligned} \tag{19}$$

where $Power^{BS}_{DIS,h}$ and $Power^{BS}_{CH,h}$ are the BSS discharge and charge, respectively. $Power^{losses}_{b,h}$ and $NR$ are the active MG loss of the $b$th line and the number of lines.

#### 3.2.3. Voltage Limits

The root mean square (rms) value of the bus voltage $\left(Voltage^{bus}\right)$ must not decrease below the minimum voltage $Voltage^{bus}_{min}$ which is set to 0.95 p.u. value, and do not increase over the maximum voltage value $Voltage^{bus}_{max}$ which is set to 1.05 p.u. in this study, as represented in Equation (20).

$$Voltage^{bus}_{min} \leq Voltage^{bus} \leq Voltage^{bus}_{max} \tag{20}$$

#### 3.2.4. Carrying Current Capacity Limit

The current flowing in each branch ($TI^{line}_{RMS}$) must not exceed the maximum carrying capacity of the branch ($TI^{line-max}_{RMS}$), as given by Equation (21).

$$TI^{line}_{RMS} \leq TI^{line-max}_{RMS} \tag{21}$$

#### 3.2.5. Energy Storing Limits

BSSs have many limits that must be considered in this study, such as the charging power ($Power^{BS}_{CH,h}$) and the discharging power ($Power^{BS}_{DIS,h}$), as represented by Equations (22) and (23).

$$Power^{BS}_{CH,h} \leq Power^{BS-max}_{CH,h}, \ \forall h \leq H \tag{22}$$

$$Power^{BS}_{DIS,h} \leq Power^{BS-max}_{DIS,h}, \ \forall h \leq H \tag{23}$$

The state of charge of BSS ($BSOC^h$) must be restricted by its minimum ($BSOC^h_{min}$) and maximum ($BSOC^h_{max}$) thresholds as specified in Equation (24) with respect to the efficiency of charge ($\eta^{Bat}$) of the BSS. The current $BSOC^h$ is a function of the previous $BSOC^{h-1}$ and the charge and discharge capacities at $h$ as specified in Equation (25). The initial $BSOC$ $\left(BSOC^{in}\right)$ is considered at $h$ = 1, as specified in Equation (25).

$$BSOC^h_{min} \leq BSOC^h \leq BSOC^h_{max}, \ \forall h \leq H \tag{24}$$

$$BSOC^h = \begin{cases} BSOC^{in} + \Delta h \, \eta^{Bat} \, Power^{BS}_{CH,h} - \Delta h \, Power^{BS}_{DIS,h}, & h = 1 \\ BSOC^{h-1} + \Delta h \, \eta^{Bat} \, Power^{BS}_{CH,h} - \Delta h \, Power^{BS}_{DIS,h}, & \forall h \geq 2, \ h \in H \end{cases} \tag{25}$$

At the end of the day, the $BSOC^h$ should be the same $BSOC^{in}$ to maintain $BSOC^{in}$ is always constant, as represented by Equation (26).

$$BSOC^h = BSOC^{in}, \ h = H \tag{26}$$

Equation (27) demonstrates that when the efficiency $\eta^{Bat}$ is taken into account, the discharge power is always equal to the charge power.

$$\textstyle\sum_{t=1}^{T} Power^{BS}_{DIS,h} = \displaystyle\sum_{t=1}^{T} Power^{BS}_{CH,h} \cdot \eta^{Bat} \tag{27}$$

### *3.3. Harris Hawks Optimizer*

Heidari et al. presented the Harris hawks optimizer (HHO) in 2019 [53,54], a recent population-based optimization method. A flock of hawks will startle its prey, usually a rabbit, by attacking it from several angles. A leader hawk encircles the victim in this synchronized attack. The hawks' abilities to alter their hunting strategies in response to the hunting environment and the rabbits' struggle to avoid capture. The three stages of Harris hawk hunting are exploration, the transition from exploration to exploitation, and globalization of search (exploitation). The hawks scour the immediate region throughout their excursion, using their outstanding vision to find rabbits. The first tactic relies on all the hawks cooperating to shock the rabbit, whereas the second focuses on having the hawks' leader attack the rabbit following the rabbit's abilities. Hawks may choose where to sit depending on the locations of nearby hawks, as expressed in (28), provided that $\alpha < 0.5$ is fulfilled and each choice is given an equal probability.

$$H\ (t+1) = \begin{cases} H_R(t) - \alpha\ |H_R(t) - 2\tau\ H(t)| & Q \geq 0.5 \\ (H_{\ Best}(t) - \left(\frac{1}{M}\sum_{i=1}^{M} H_i(t)\right)\right) - \varphi\ (LB + \varnothing\ (UB - LB) & Q < 0.5 \end{cases} \quad (28)$$

where $H(t+1)$ denotes the hawks' location vector at iteration $t+1$, $H(t)$ denotes the Hawks' location vector during iteration $t$. The place of the prey is represented by $H_{Best}(t)$; the total number of hawks is represented by $M$; and the random values $\alpha$, $\tau$, $\varphi$, $\varnothing$, and $Q$ are generated from the range [0, 1].

HHO can transition from exploration to exploitation by using rabbit escape energy ($E$):

$$E = 2\ E_o\left(1 - \frac{t}{T}\right) \quad (29)$$

$E_o$ is the rabbit's initial random energy, which is calculated for each iteration from the range [−1, 1], and $T$ stands for the maximum number of iterations. According to the rabbit escape scenario, Harris hawks can hunt using either a hard besiege or a delicate attachment method. The rabbit attempts to escape the gentle besiege with $p \geq 0.5$ and $|E| \geq 0.5$ but finally fails. These attacks involve the hawks softly around the rabbit to make it more tired before coming in from nowhere. Equations (30) and (31) are used to express this behavior.

$$H(t+1) = \Delta H(t) - E|(J \cdot H_{Best}(t)) - H(t)| \quad (30)$$

$$\Delta H(t) = H_{Best}(t) - H(t) \quad (31)$$

where $J$ is the rabbit's random escape strength and $\Delta H(t)$ is the difference between the $H_{Best}(t)$ and $H(t)$ in iteration $t$.

The rabbit is worn out and has minimal escape energy throughout the difficult besiege, where $r \geq 0.5$ and $|E| < 0.5$. As a result, the hawks seldom ever surround the rabbit to launch an unexpected assault. This behavior is represented by Equation (32).

$$H(t+1) = H_{Best}(t) - E|\Delta H(t)| \quad (32)$$

Further, more advanced soft and hard siege techniques are possible, as mentioned in [53]. For further information regarding the HHO, the reader could refer to [53,54].

## 4. Numerical Results and Their Discussion

To more effectively solve the uncertainty parameters and comprehend the implications of parameter uncertainty on the result, the stochastic technique makes use of many scenarios and the corresponding probability. Using historical data, 1000 scenarios have been developed to simulate the uncertainty of each PV and WT, load demand, and market price change. Then, in order to shorten calculation time, the number of PV, WT, demand, and market price scenarios is reduced to the ten most-probable scenarios using a scenario reduction technique based on the FCM clustering algorithm.

Following the scenario reduction technique, the clustering powers of the PV installed in bus 7 and their probabilities are shown in Figure 4. The clustering power of the PV systems installed in buses 9, 11, and 21 is shown in Figure 5, along with their probabilities. In addition, Figure 6 displays the clustered power of PV installed in bus 33 and their probabilities.

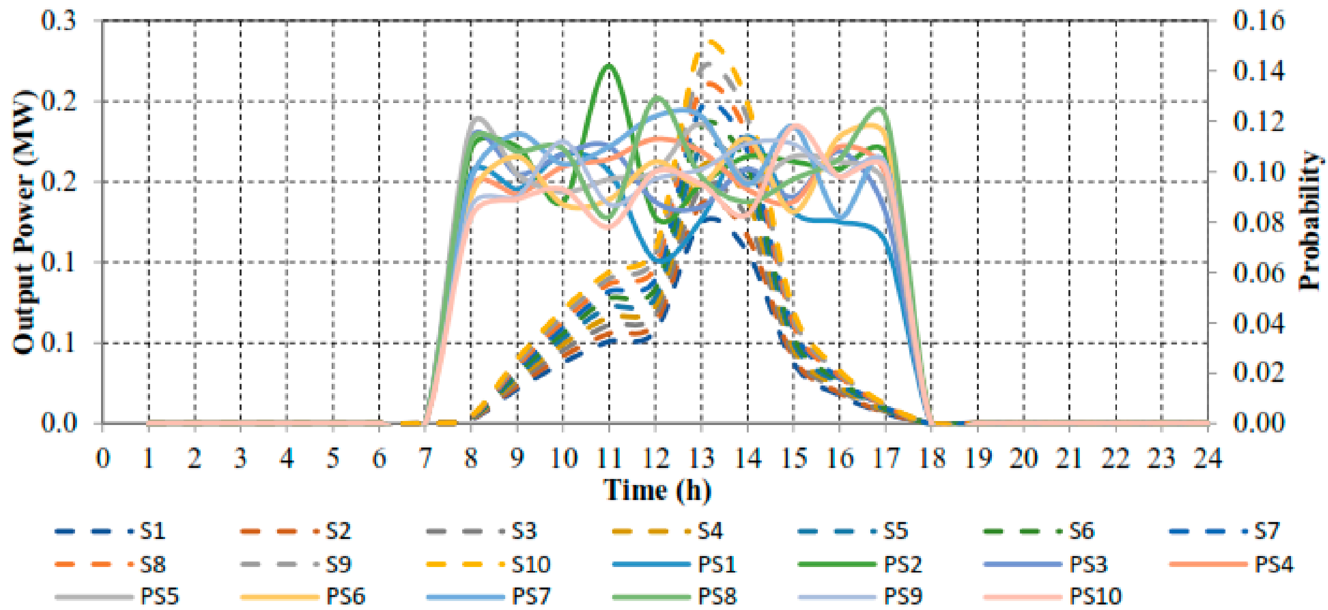


**Figure 4.** Hourly power scenarios and their probabilities of PV installed in bus 7.

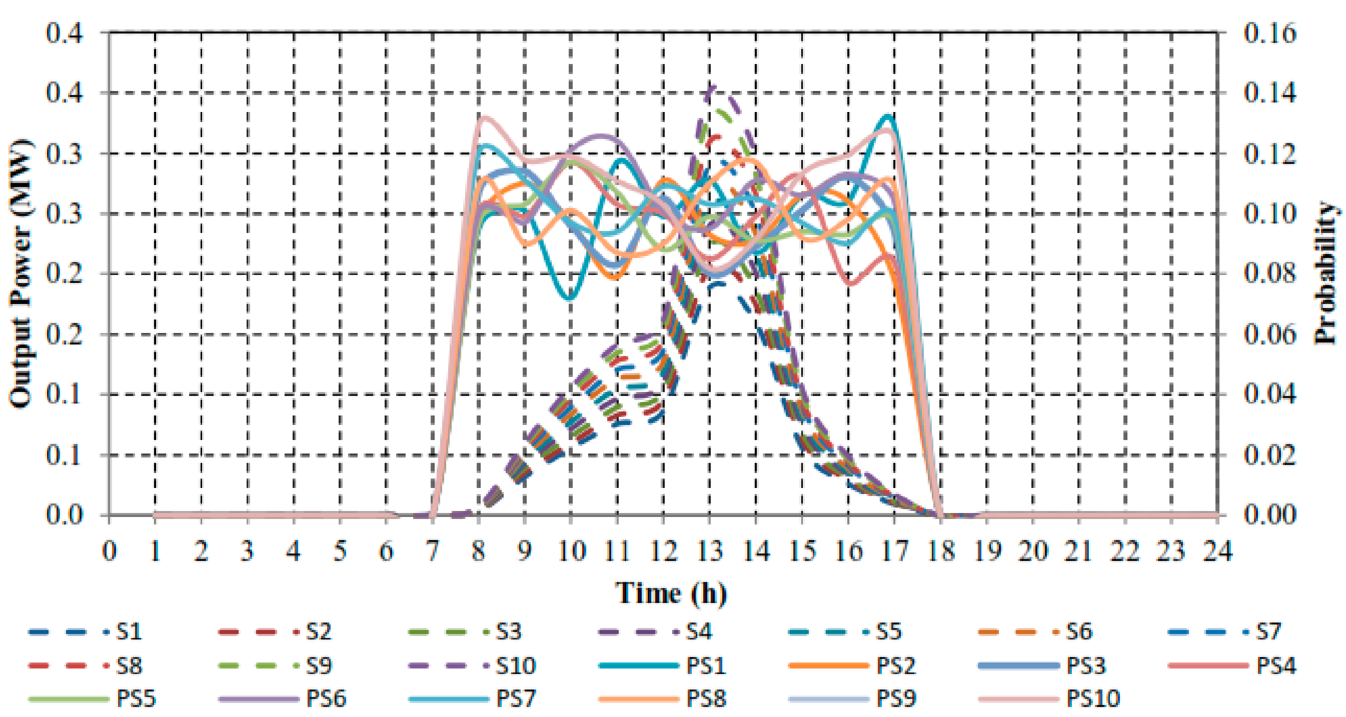


**Figure 5.** Hourly power scenarios and their probabilities of PVs installed in buses 9, 11, and 21.

The clustering powers of the WTs placed in buses 6 and 31, as well as their probabilities, are presented in Figure 7. The WT systems installed in buses 12 and 18 have the same output power because they have the same historical data and size. The clustering powers of the WT placed in buses 12 and 18 and their probabilities are shown in Figure 8. The clustering powers of WT installed in bus 19 are shown in Figure 9 and their probabilities. The demand for electricity is never uniform; it changes every hour. The maximum load in the MG under study is 3.715 MW; the hourly load is a percentage of the maximum load. The key factor contributing to the complexity of MG management is the inherent variability of the load that customers need. As a result, this analysis takes the electrical load's uncertainty into account. Figure 10 depicts the power load clustering scenarios and their probabilities for each hour of the day. Figure 11 illustrates the market price clustering scenarios and their probabilities for each hour of the day.

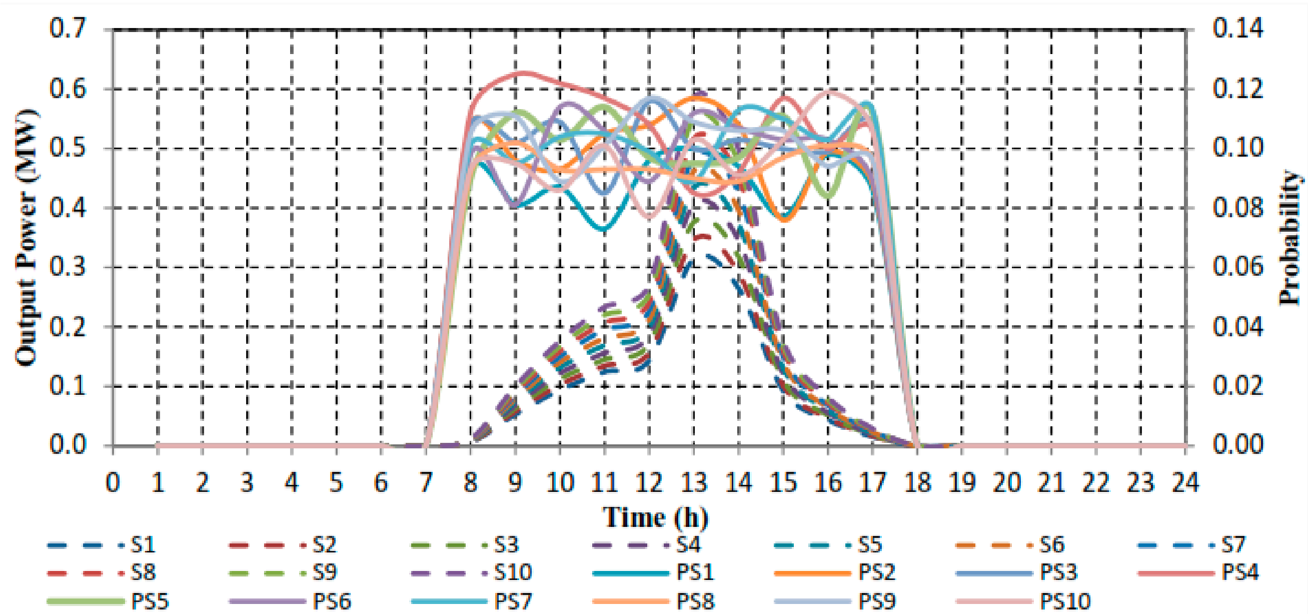


**Figure 6.** Hourly power scenarios and their probabilities of PV installed in bus 33.

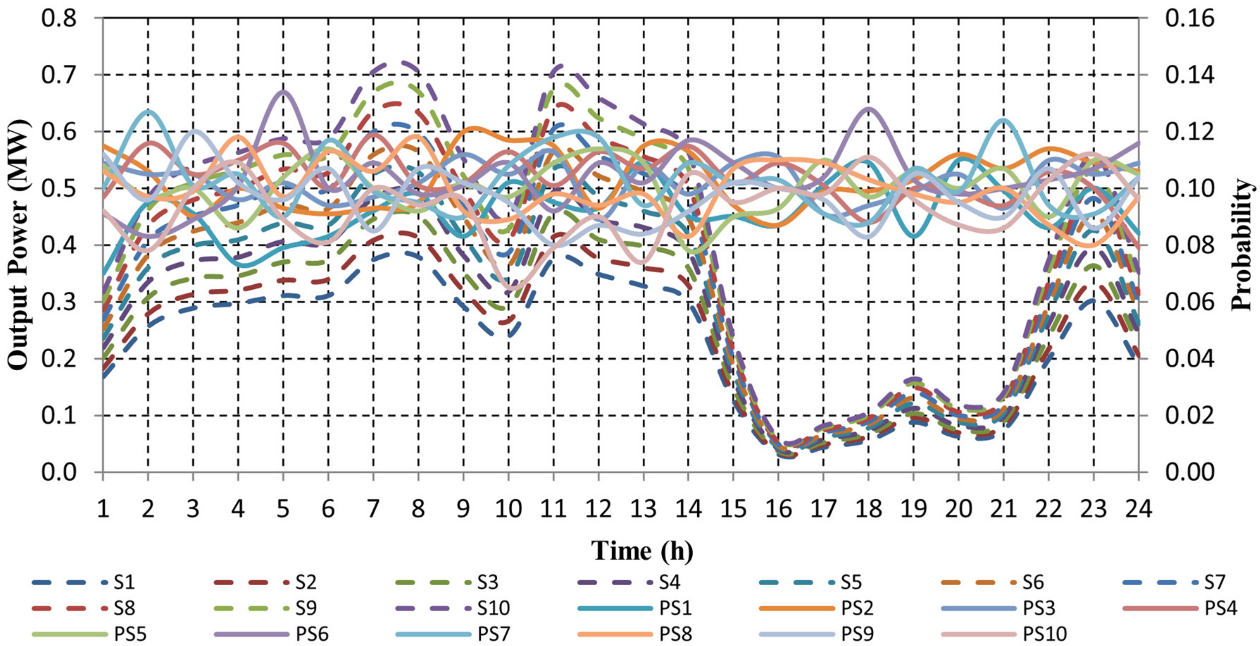


**Figure 7.** Hourly power scenarios and their probabilities of WTs installed in buses 6 and 31.

The system voltage fluctuations and total power loss will be adversely affected by the placement of the BSS in the MG. Therefore, developing an optimal approach for choosing the appropriate location and size for the BSS is essential. The SCR and HC of RESs must be improved, and the operation cost of the MG must be minimized while taking into account operational microgrid constraints such as PV and WT uncertainty, electrical load variation, market price fluctuations, RES power limits, power balance limits, voltage limits, line capacity constraints, and energy storage limits. In order to maximize SCR to 100% and reduce MG operation cost while considering operational MG limits, BSS is added to each bus, boosting its capacity. This plan was carried out using the HHO, including the following steps:

- Read all RES, BSS, and MG data in Step 1.
- Execute the MG's load flow in Step 2 and store the results.
- In Step 3, start the HHO program.
- Step 4 attaches the BSS to each bus using various power and energy values.
- Step 5: Run the load flow and obtain the value of the objective function for each size.
- Step 6: Repetition of Steps 4 and 5 will help to determine the best BSS size and location for the most remarkable (the best global) objective function.

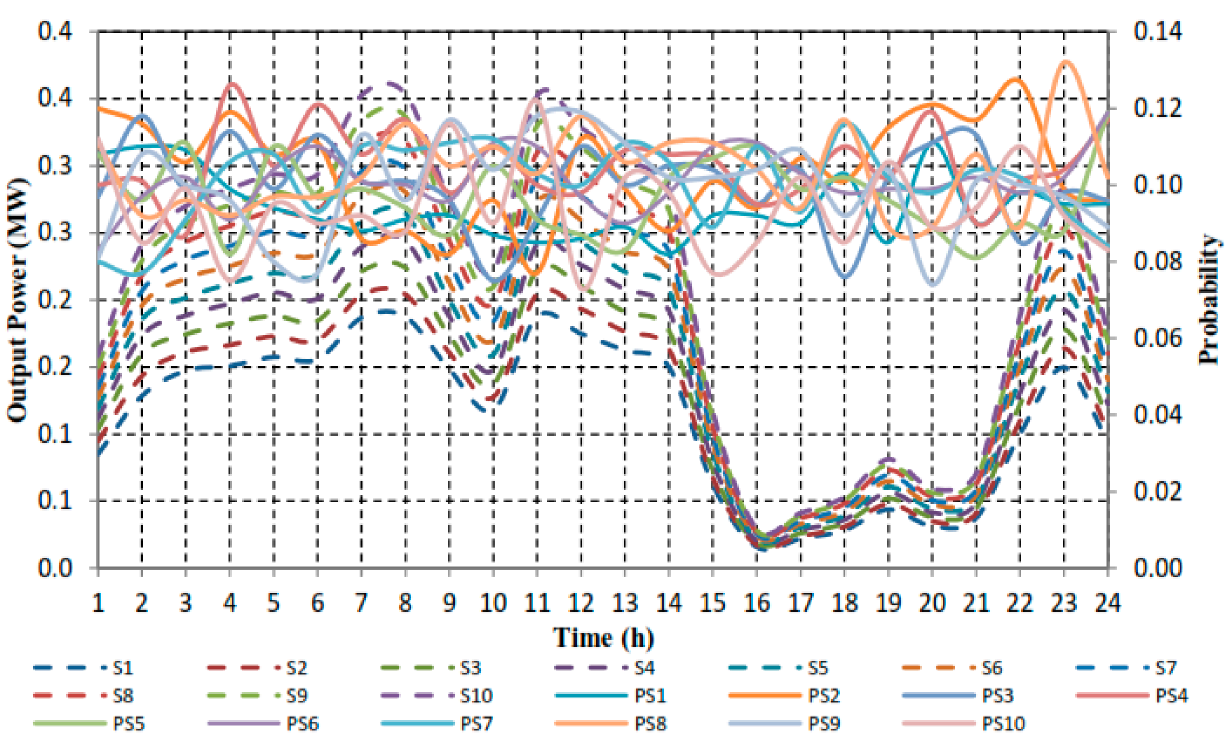


**Figure 8.** Hourly power scenarios and their probabilities of WTs installed in buses 12 and 18.

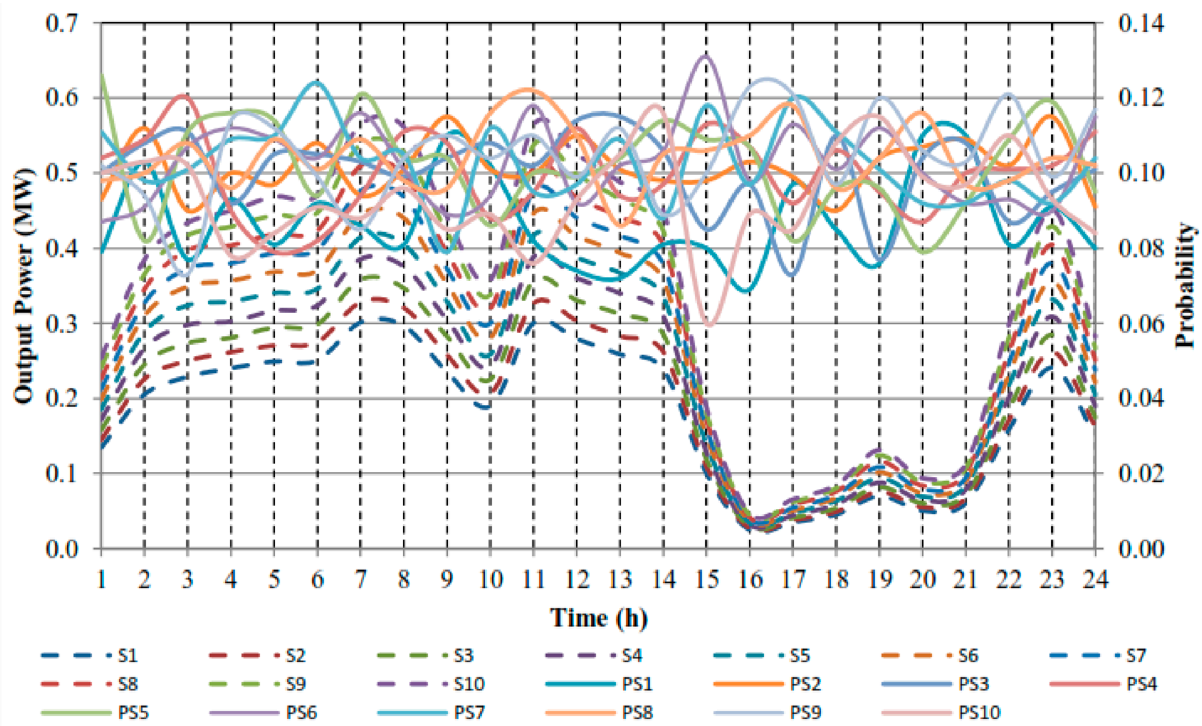


**Figure 9.** Hourly power scenarios and their probabilities of WTs installed in bus 19.

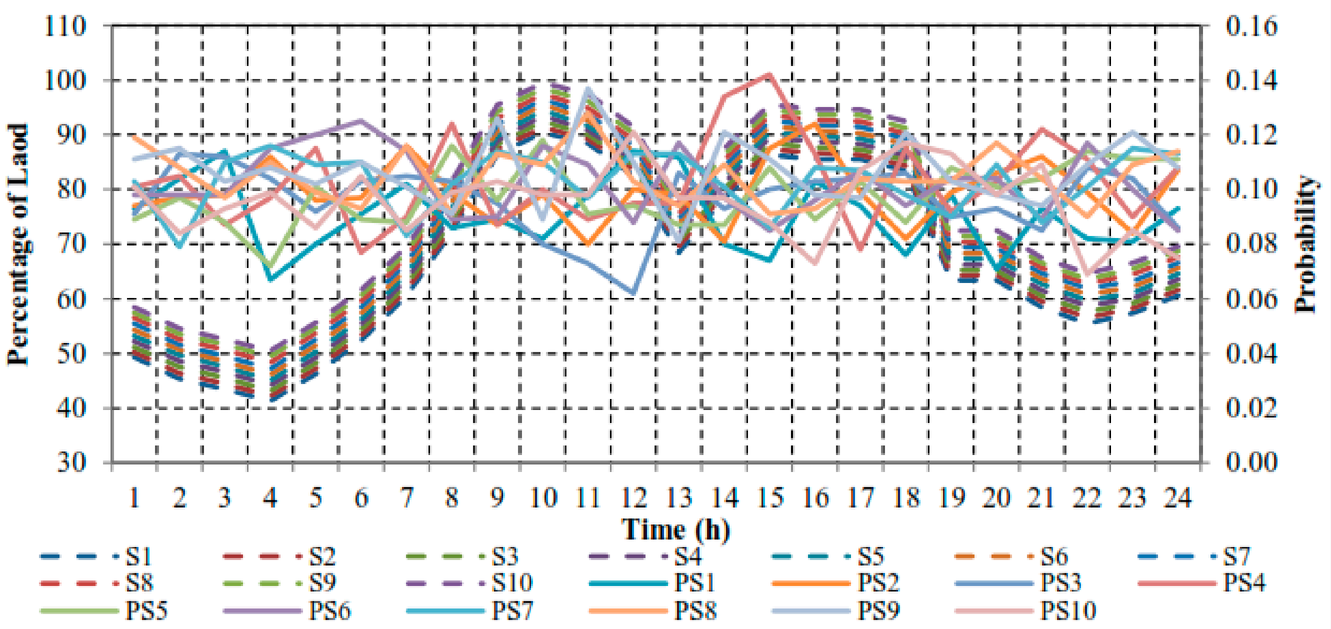


**Figure 10.** Hourly generated electrical load scenarios and their probabilities.

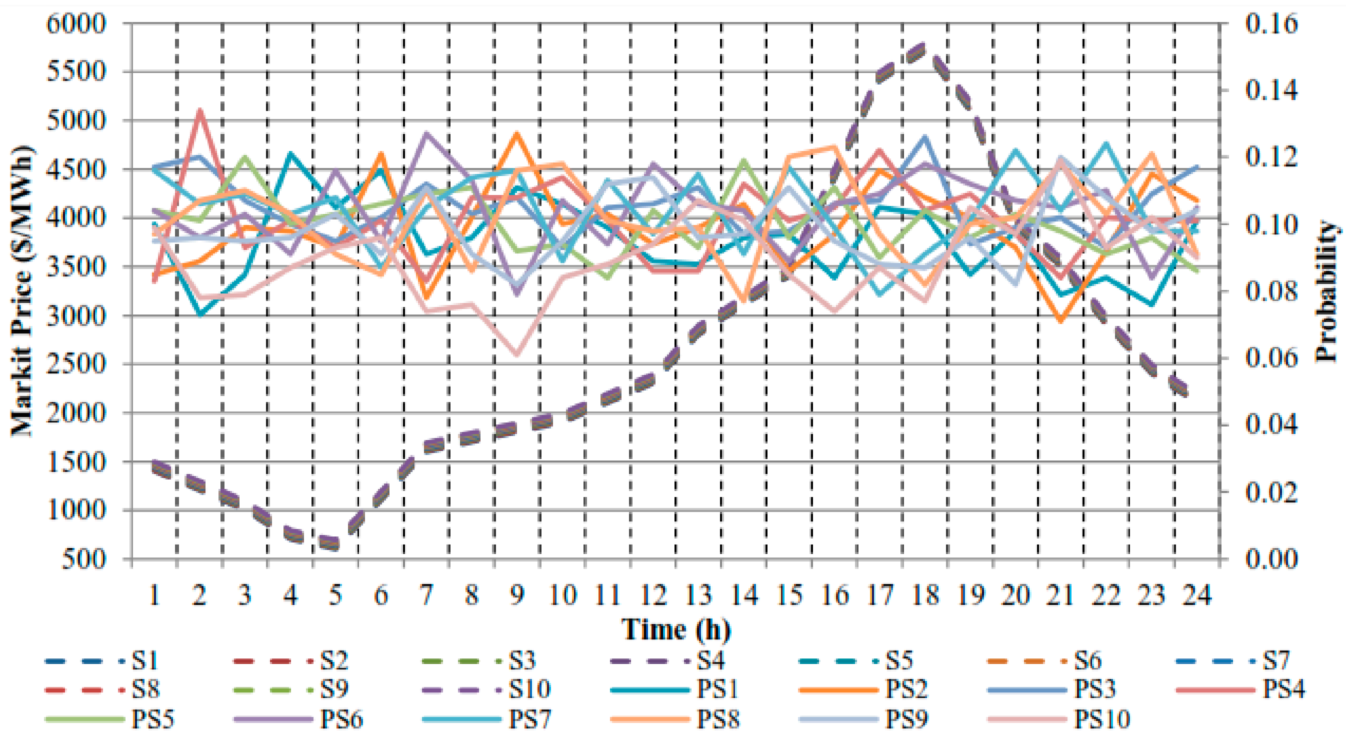


**Figure 11.** Hourly generated market price scenarios and their probabilities.

The PV's and WT's specified bids are set to 2.8 (USD/kWh) and 1.72 (USD/kWh), respectively [2]. Table 2 provides information on the cost, efficiency, and durability of the NaS battery used in this study [2,13].

**Table 2.** Efficiency, cost factors, and lifecycle of NaS batteries [2,13].

| Battery | Capital Power Cost (USD/kW) | Capital Energy Cost (USD/kWh) | Efficiency (%) | Lifecycle | Lifetime (Years) |
|---|---|---|---|---|---|
| NaS | 350 | 300 | 95 | 4500 | 15 |

The appropriate position and size of the NaS batteries are given in Table 3 in order to maximize SCR and lower the operating cost of the MG. The MG's cost-effectiveness is established by lowering running expenses and maximizing the system's self-consumption of PV and WT after determining the NaS's optimal position.

**Table 3.** Optimal allocation of the NaS battery.

| Battery | Location | Power (MW) | Energy (MWh) |
|---|---|---|---|
| NaS | 6 | 2.06 | 12.37 |

Figure 12 shows the SCR of WTs and PVs on an hourly basis without the NaS battery. It is clear that neither of them always consumes themselves entirely. The self-consumption of WT varies between 81.8% and 91.4% from hours 3 to 5, and it equals 90.1% in hour 7. Additionally, the self-consumption of PV varies between 31.8% and 66.2% from hour 13 to hour 14. Undoubtedly, the MG operator wants to increase the WT and PV's self-consumption to 100% at all times of the day in order to make them more commoditized and accessible as options for electricity generation. After adding the NaS battery, the WT and PV self-consumption equals 100% during the entire day. The NaS positively affects RES self-consumption in this regard.

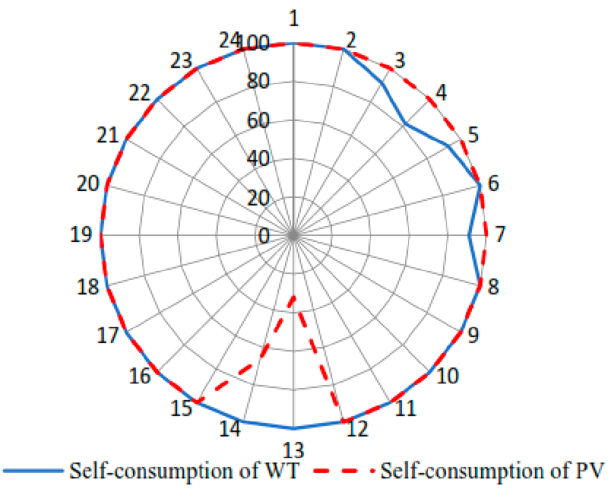


**Figure 12.** The self-consumption of PV and WT with no NaS battery connected.

Figure 13 shows the hourly HC of RESs in the investigated MG without and with one NaS battery. As shown in this figure, the HC of RESs increases from 8.863 MW in the absence of a NaS battery to 10.213 MW, improving the HC of RESs.

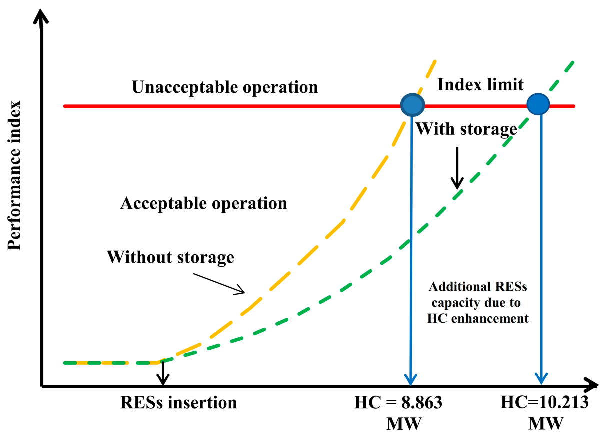


**Figure 13.** HCRES in the studied MG.

The operational costs of the MG with and without the NaS battery are shown in Table 4, which provides the MG economic analysis after determining the appropriate NaS battery allocation from an economic perspective.

**Table 4.** Impact of the NaS battery on the MG from an economic perspective.

| Case | With No NaS | With NaS |
|---|---|---|
| Operation cost (USD/day) | 183,645.3 | 138,550.7 |
| $BS_c$ (USD) | ----- | 4,432,225.5 |
| $RN_{BSS}$ | ----- | 3 |
| Cost NaS/day (USD/day) | ----- | 1457.2 |
| Total operating cost/day (USD/day) | 183,645.3 | 140,007.9 |
| Saving (%) | ----- | 23.8 |

The total cost per day for the project includes the capital and replacement costs for the NaS, as shown in Table 4. The project life span in this analysis is 25 years, and the interest rate is 0.08. In order to know the NaS batteries' replacement number over the project's duration, the batteries' expected lifetimes are calculated. The saving percentage is determined with respect to the base scenario while keeping in mind the life cycles of the NaS provided in Table 2 and the overall number of cycles completed through the NaS $\left(Battery_{cycles}\right)$ per year. The results showed that adding NaS to the MG considerably reduces operating expenses.

The optimal output powers for the main grid, PV, WT, and NaS at each hour of the day are presented in Figure 14. Figure 15 shows the NaS battery's SOC for each hour of the day. In order to comply with the MG constraints, Figures 14 and 15 indicate that the battery storage is charged when the energy price is low and the overall load is not high, such as the first periods from hour 1 to hour 7. When the energy market price is high, such as between hours 16 and 21, the battery storage begins to discharge in order to lower the MG's operating costs. Figure 14 clearly shows that the BSS is charged in the early periods because of the low market price and light total load. Figure 16 shows that the SOC of the battery changed from 0% at hour 1 to 100% at hour 14.

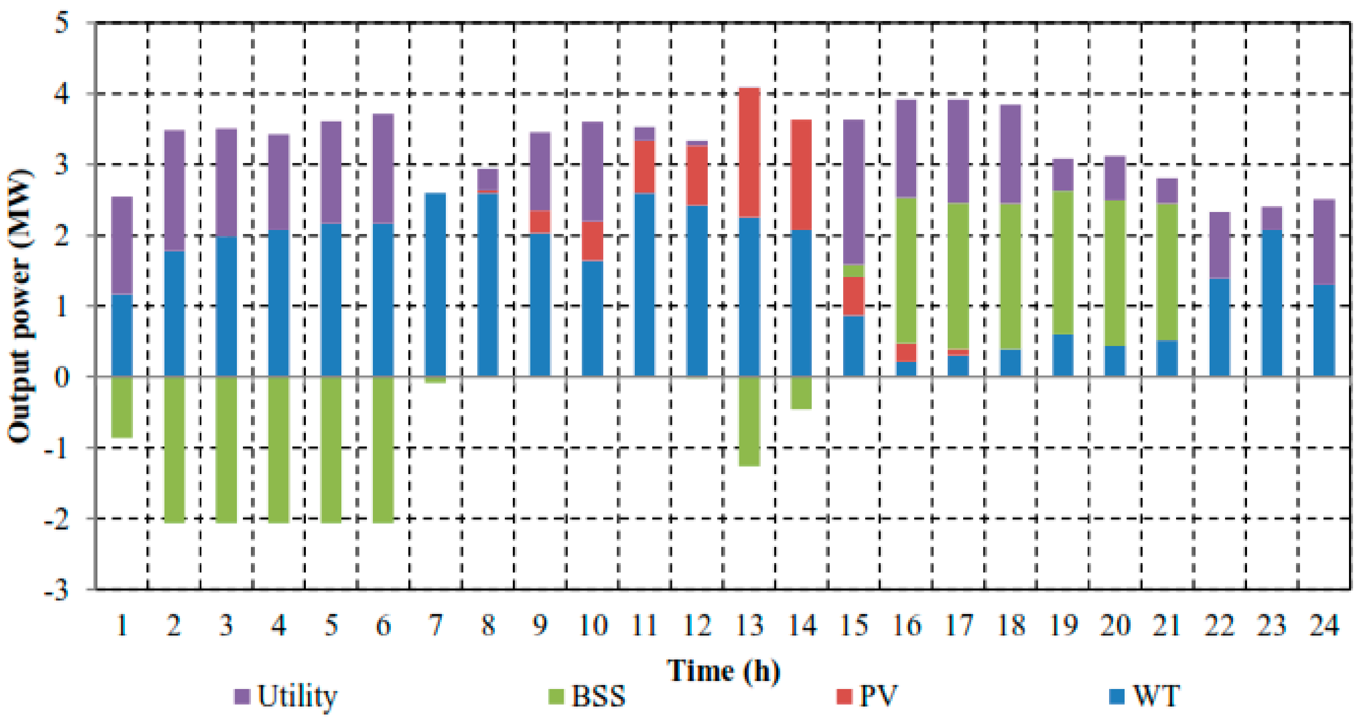


**Figure 14.** Optimal hourly power of the main grid, WT, PV, and the BSS.

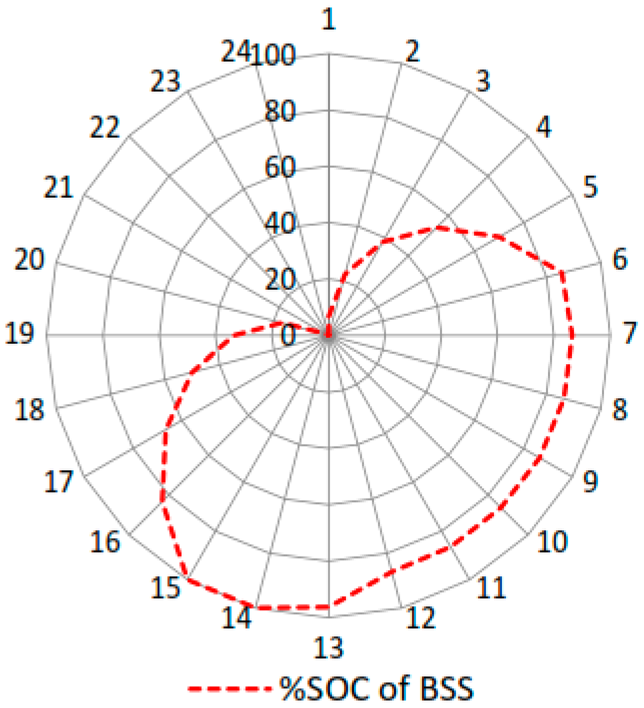


**Figure 15.** SOC of the BSS.

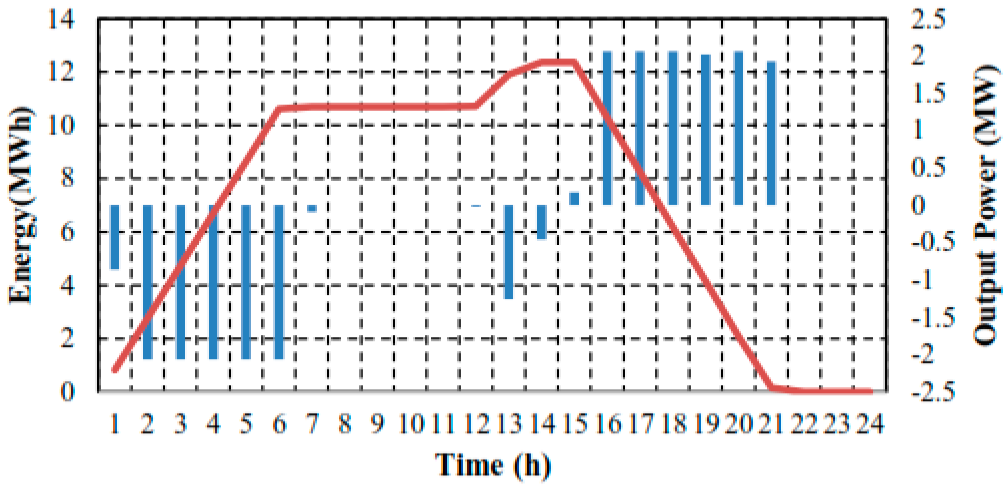


**Figure 16.** Charge and discharge power and SOC of the BSS.

The transformer between the primary grid and the considered MG provides power for the MG's electrical load. When the output power of the RESs diminishes, more electricity is drawn from the main grid and delivered to the MG via the transformer. The transformer in the MG under study has a rated capacity $S_{Tr}^{rated}$ and rated power $(Power_{Tr}^{rated})$ of 3500 kVA and 2976 kW, respectively. Transformer overloads may occur when the overall output power of the RESs is low and the overall demand is high. Figure 17 shows the transformer's load rate both with and without storage. It also shows the transformer's maximum rated power.

Power reversal occurs when there is a more significant difference between the total output power of all RES and the entire load, such as between hours 12 and 14, where MG operates without storage. Transformer overloads can also occur when there is a high overall demand and a low overall output power from RESs, as shown in Figure 17 for the case where MG runs without storage throughout the hours from hour 16 to hour 18. The transformer load rate does not increase above its rated power after adding the BSS. It is necessary to reduce the transformer load rate because the ESS relocated the load from on-peak to off-peak hours of the day. As a result, it will delay the reinforcement of the transformer size.

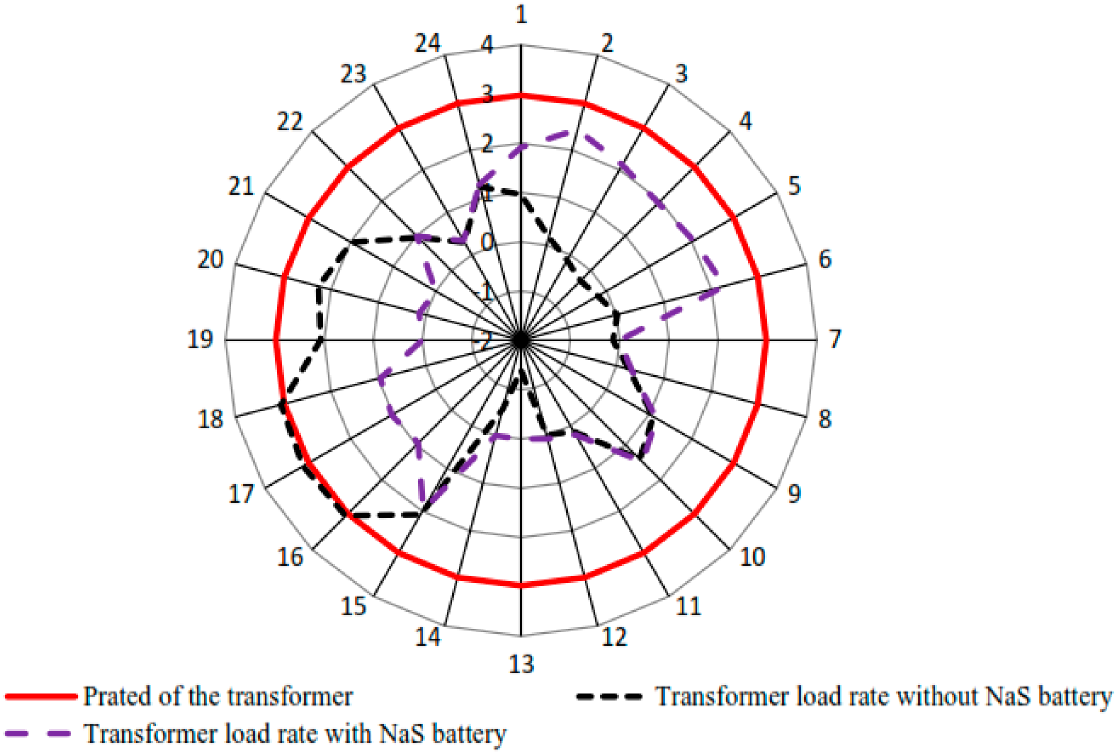


**Figure 17.** The transformer's rated power and load rate with and without storage.

Additionally, Figure 18 illustrates how the MG's power losses in the early phases increase compared to the basic situation. Another interesting finding from Figure 16 is that the SoC of the BSS is continuous from hour 8 to hour 12. The power losses decreased from hour 15 to hour 19 when the BSS discharged. The MG's overall power losses for the day nevertheless decreased from 1493.2 kW to 1471.1 kW after the addition of the BSS. The BSS affects the MG's overall power losses in this way.

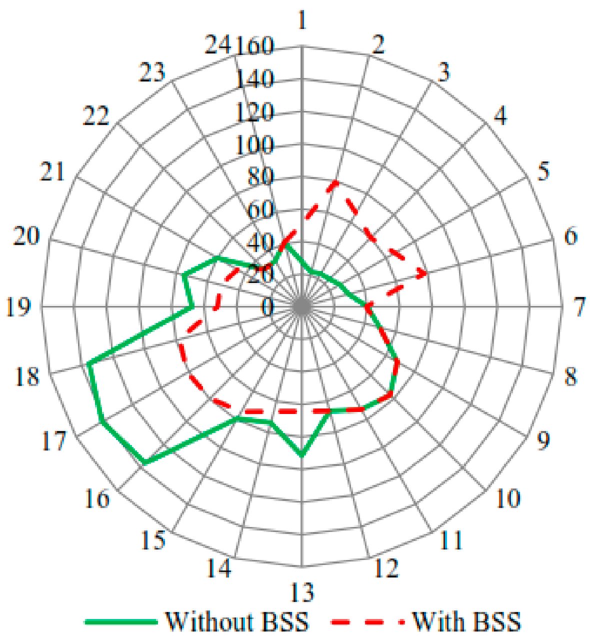


**Figure 18.** Hourly power losses (kW).

Figure 19 depicts the voltage profile of the MG at four distinct times following the daily load profile: at $h$ = 4 (low loading), $h$ = 10 (very high loading), $h$ = 14 (high loading), and $h$ = 21 (medium loading). It is crucial to note from Figure 19a that the voltage profile of the MG at the fourth hour in the absence of a BSS is close to 1 per unit at all buses because of the light load on each bus. Due to low market pricing and loads on each bus during the integration of a BSS, the BSS is charged during the fourth hour, resulting in a lower voltage profile for the MG than in the base scenario while taking into account the voltage limitations on each bus. Figure 19b indicates that the voltage profile of the MG at the 10th hour is the same in all cases due to the integrated BSS's constant SOC. As seen in Figure 19c, when the BSS is charged at this hour, the voltage profile of the MG at $h$ = 14 decreases. Figure 19d makes it clear that the MG's voltage profile at $h$ = 21 was superior to the base case since the BSS is discharged at this time. In this way, the BSS improved the voltage profile of the MG at these specific instances.

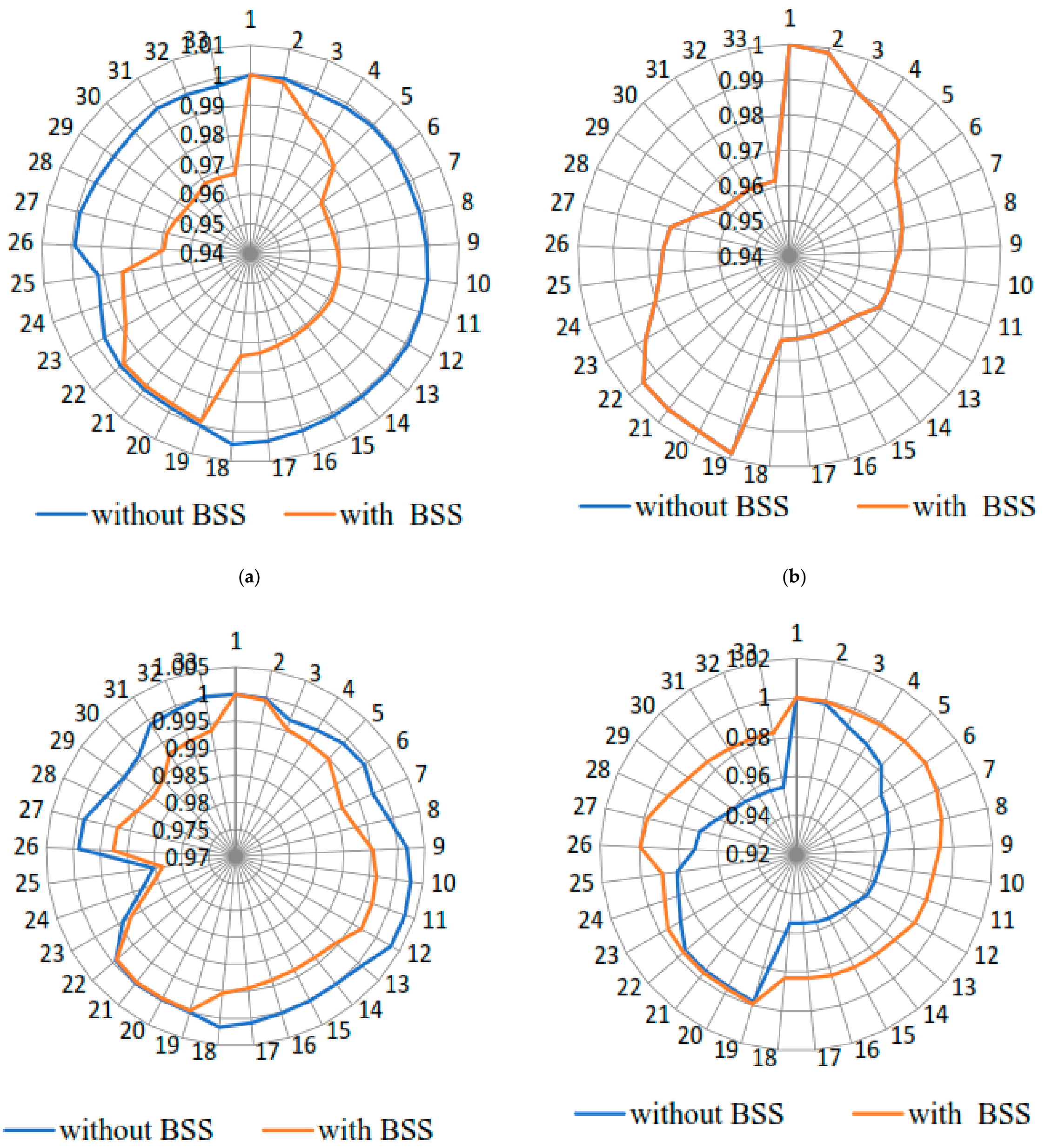


(**a**) (**b**) (**c**) (**d**)

**Figure 19.** Bus voltage for each bus at four selective periods at: (**a**) $h$ = 4, (**b**) $h$ = 10, (**c**) $h$ = 14, and (**d**) $h$ = 21.

To sum up, many research studies [54–62] have examined the economic MG operational costs using different characteristics. Some studies ignored uncertainty parameters and focused on economics. Other researchers considered some uncertainty parameters but ignored others. Table 5 presents a comparison between some studies and the proposed study from where the renewable energy resources included in the MG, the uncertainty parameters, the percentage of saving, and the studied topics discussed in the paper. The methodology used in this study is generic and effective, as seen in Table 5.

**Table 5.** Overview of recent research works addressing the planning and operation of MGs.

| Ref. | Renewables Used | | Uncertainty | | | | Topics Studied | | | | | | |
|---|---|---|---|---|---|---|---|---|---|---|---|---|---|
| | PV | WT | PV | WT | Demand | Market Price | Total Operation Cost Studied | Total Operation Cost Saving% | SCR of RESs | HC | Transformer Load Rate | Voltage Profile | Power Losses |
| [55] | √ | √ | √ | √ | X | X | √ | 7.00 | X | X | X | X | X |
| [56] | √ | √ | X | X | X | X | √ | 16.80 | √ | X | √ | √ | √ |
| [57] | √ | X | √ | X | √ | X | √ | 20.00 | √ | X | X | √ | X |
| [58] | √ | √ | √ | √ | X | X | √ | 6.99 | X | X | X | X | X |
| [59] | √ | √ | X | X | √ | X | √ | 20.50 | X | X | X | X | X |
| [60] | √ | X | X | X | X | X | √ | 25.10 | X | X | X | X | X |
| [61] | √ | √ | √ | √ | √ | X | √ | 10.00 | X | X | X | X | X |
| [62] | X | √ | X | √ | √ | X | √ | 4.50 | X | X | X | √ | X |
| [63] | √ | √ | X | X | √ | X | √ | 3.20 | X | X | X | X | √ |
| Proposed | √ | √ | √ | √ | √ | √ | √ | 23.80 | √ | √ | √ | √ | √ |

## 5. Conclusions

An optimization model is suggested in this work to identify the optimal location and size of a BSS in the grid-connected MG while taking into account the uncertainty of RESs, variations in electrical loads, and fluctuations of market prices. This is carried out in order to maximize RES self-consumption rate, RES hosting capacity, and MG operating cost minimization. To address the economic sustainability of the BSS and to understand the hosting capacity of RESs in the MGs as well as the load rate of the transformer that connects the main grid and the MG, decision-makers can efficiently use the provided optimization framework. The main conclusions of the paper are summarized as follows:

- The study demonstrated that the BSS has a beneficial effect on the RES' SCR, showing that after adopting the BSS, the RES' SCR achieved 100% at all times of the day.
- Furthermore, it has been shown that adding NaS batteries improves the HC of RESs greatly, as shown by the increase in HCRES from 8.863 MW in the absence of a NaS battery to 10.213 MW.
- The results showed that the optimal placing of the BSS in the MG considerably reduces its overall operating costs in terms of the cost of operation. The MG's operating costs were 183,645.3 (USD/day) before the BSS was installed; the MG's operating costs were 140,007.9 (USD/day) after the BSS was installed. As a result, the savings percentage rate was 23.8%.
- The optimal BSS placement helps reduce the overall active power losses.
- Transformer overloads are likely to occur within a few hours due to the high load and low output power of RESs during these hours. Through comparison, we have found that the BSS could shift the load from the day's on-peak hours to the off-peak hours, which is essential in lowering the transformer load rate. It is, therefore, used to delay reinforcing the transformer.

Finally, future research should focus on the exploration of the hybridization of different BSSs in MGs to be more techno-economically effective while also enhancing the performance of the MG and lowering operational costs. In addition, in future works, all costs will be considered.

**Author Contributions:** M.M.A., M.H.M. and S.H.E.A.A. designed the problem under study; Z.M.A. and M.M.A. performed the simulations and obtained the results; M.M.A. and M.H.M. analyzed the obtained results; M.M.A., M.H.M. and S.H.E.A.A. wrote the paper, which was further reviewed by Z.M.A. All authors have read and agreed to the published version of the manuscript.

**Funding:** This project was supported by the Deanship of Scientific Research at Prince Sattam Bin Abdulaziz University under the research project (PSAU2022/01/19413).

**Data Availability Statement:** The data presented in this study are available on request from the corresponding author.

**Acknowledgments:** The authors acknowledge the Deanship of Scientific Research at Prince Sattam Bin Abdulaziz University for supporting this research project (PSAU2022/01/19413).

**Conflicts of Interest:** The authors declare no conflict of interest.

## References


1. Debouza, M.; Al-Durra, A.; EL-Fouly, T.H.M.; Zeineldin, H.H. Survey on microgrids with flexible boundaries: Strategies, applications, and future trends. *Energies* **2022**, *205*, 107765. [CrossRef]
2. International Energy Agency (IEA). *Electricity Market Report 2022*; International Energy Agency: Paris, France, 2022.
3. Caparrós Mancera, J.J.; Saenz, J.L.; López, E.; Andújar, J.M.; Segura Manzano, F.; Vivas, F.J.; Isorna, F. Experimental analysis of the effects of supercapacitor banks in a renewable DC microgrid. *Appl. Energy* **2022**, *308*, 118355. [CrossRef]
4. Shang, Z.; Hossain, M.; Wycisk, R.; Pintauro, P. Poly(phenylene sulfonic acid)-expanded polytetrafluoroethylene composite membrane for low relative humidity operation in hydrogen fuel cells. *J. Power Sources* **2022**, *535*, 231375. [CrossRef]
5. Abo-Khalil, A.G.; Alobaid, M. A Guide to the Integration and Utilization of Energy Storage Systems with a Focus on Demand Resource Management and Power Quality Enhancement. *Sustainability* **2023**, *15*, 14680. [CrossRef]
6. Villanueva-Rosario, J.A.; Santos-García, F.; Aybar-Mejía, M.E.; Mendoza-Araya, P.; Molina-García, A. Coordinated ancillary services, market participation and communication of multi-microgrids: A review. *Appl. Energy* **2022**, *308*, 118332. [CrossRef]
7. Xuanyue, S.; Wang, X.; Wu, X.; Wang, Y.; Song, Z.; Wang, B.; Ma, Z. Peer-to-peer multi-energy distributed trading for interconnected microgrids: A general Nash bargaining approach. *Int. J. Electr. Power Energy Syst.* **2022**, *138*, 107892. [CrossRef]
8. Stetz, T.; Marten, F.; Braun, M. Improved Low Voltage Grid-Integration of Photovoltaic Systems in Germany. *IEEE Trans. Sustain. Energy* **2013**, *4*, 534–542. [CrossRef]
9. Kabiri, R.; Holmes, D.G.; McGrath, B.P.; Meegahapola, L.G. LV Grid Voltage Regulation Using Transformer Electronic Tap Changing, With PV Inverter Reactive Power Injection. *IEEE J. Emerg. Sel. Top. Power Electron.* **2015**, *3*, 1182–1192. [CrossRef]
10. Tonkoski, R.; Lopes, L.A.; El-Fouly, T.H. Coordinated active power curtailment of grid connected PV inverters for overvoltage prevention. *IEEE Trans. Sustain. Energy* **2011**, *2*, 139–147. [CrossRef]
11. Yao, E.; Samadi, P.; Wong, V.W.S.; Schober, R. Residential Demand Side Management Under High Penetration of Rooftop Photovoltaic Units. *IEEE Trans. Smart Grid* **2015**, *7*, 1597–1608. [CrossRef]
12. Samadi, A.; Shayesteh, E.; Eriksson, R.; Rawn, B.; Söder, L. Multi-objective coordinated droop-based voltage regulation in distribution grids with PV systems. *Renew. Energy* **2014**, *71*, 315–323. [CrossRef]
13. Rawa, M.; Abusorrah, A.; Al-Turki, Y.; Mekhilef, S.; Mostafa, M.H.; Ali, Z.M.; Aleem, S.H.E. Optimal Allocation and Economic Analysis of Battery Energy Storage Systems: Self-Consumption Rate and Hosting Capacity Enhancement for Microgrids with High Renewable Penetration. *Sustainability* **2020**, *12*, 10144. [CrossRef]
14. Nudell, T.R.; Brignone, M.; Robba, M.; Bonfiglio, A.; Ferro, G.; Delfino, F.; Annaswamy, A.M. Distributed control for polygeneration microgrids: A Dynamic Market Mechanism approach. *Control Eng. Pract.* **2022**, *121*, 105052. [CrossRef]
15. Guibentif, T.M.M.; Vuille, F. Prospects and barriers for microgrids in Switzerland. *Energy Strategy Rev.* **2022**, *39*, 100776. [CrossRef]
16. Alghamdi, B.; Cañizares, C. Frequency and voltage coordinated control of a grid of AC/DC microgrids. *Appl. Energy* **2022**, *310*, 118427. [CrossRef]
17. Khodadoost Arani, A.A.; Gharehpetian, G.B.; Abedi, M. Review on Energy Storage Systems Control Methods in Microgrids. *Int. J. Electr. Power Energy Syst.* **2019**, *107*, 745–757. [CrossRef]
18. Hajiaghasi, S.; Salemnia, A.; Hamzeh, M. Hybrid energy storage system for microgrids applications: A review. *J. Energy Storage.* **2019**, *21*, 543–570. [CrossRef]
19. Mostafa, M.H.; Aleem, S.H.E.A.; Ali, S.G.; Abdelaziz, A.Y.; Ribeiro, P.F.; Ali, Z.M. Robust Energy Management and Economic Analysis of Microgrids Considering Different Battery Characteristics. *IEEE Access* **2020**, *8*, 54751–54775. [CrossRef]
20. Mansouri, S.A.; Ahmarinejad, A.; Nematbakhsh, E.; Javadi, M.S.; Nezhad, A.E.; Catalão, J.P.S. A sustainable framework for multi-microgrids energy management in automated distribution network by considering smart homes and high penetration of renewable energy resources. *Energy* **2022**, *245*, 123228. [CrossRef]
21. Mostafa, M.H.; Aleem, S.H.E.A.; Ali, S.G.; Ali, Z.M.; Abdelaziz, A.Y. Techno-economic assessment of energy storage systems using annualized life cycle cost of storage (LCCOS) and levelized cost of energy (LCOE) metrics. *J. Energy Storage.* **2020**, *29*, 101345. [CrossRef]
22. Bai, H.; Tang, X.; Yuan, Z.; Li, Q.; Pan, S.; Deng, P.; Zhou, C.; Luo, N. A novel three-phase unbalanced power flow solution for islanded microgrids with distributed generations under droop controls. *Energy Rep.* **2022**, *8*, 1438–1447. [CrossRef]
23. Tomin, N.; Shakirov, V.; Kozlov, A.; Sidorov, D.; Kurbatsky, V.; Rehtanz, C.; Lora, E.E.S. Design and optimal energy management of community microgrids with flexible renewable energy sources. *Renew. Energy.* **2022**, *183*, 903–921. [CrossRef]

24. Zhang, L.; Liang, D.; Wen, Q.; Liu, H.; Liu, Y.; Li, D.; Gao, Y.; Xu, H.; Li, W.; Sun, H. Transient optimization control strategy of hybrid capacity regulating transformer. *Electr. Power Syst. Res.* **2022**, *206*, 107803. [CrossRef]
25. Hossain, E.; Perez, R.; Nasiri, A.; Padmanaban, S. A Comprehensive Review on Constant Power Loads Compensation Techniques. *IEEE Access* **2018**, *6*, 33285–33305. [CrossRef]
26. Li, Q. Design and practical application analysis of thermal management system for power battery in new energy vehicles. *Results Phys.* **2023**, *54*, 107063. [CrossRef]
27. Habib, A.; Hasan, M.; Issa, G.; Singh, D.; Islam, S.; Ghazal, T. Lithium-Ion Battery Management System for Electric Vehicles: Constraints, Challenges, and Recommendations. *Batteries* **2023**, *9*, 3. [CrossRef]
28. Li, W.; Rentemeister, M.; Badeda, J.; Schulte, D.; Sauer, D.U. Digital twin for battery systems: Cloud battery management system with online state-of-charge and state-of-health estimation. *J. Energy Storage* **2020**, *30*, 101557. [CrossRef]
29. Yang, S.; Zhang, Z.; Cao, R.; Wang, M.; Cheng, H.; Zhang, L.; Jiang, Y.; Chen, B.; Ling, H.; Lian, Y.; et al. Implementation for a cloud battery management system based on the CHAIN framework. *Energy AI* **2021**, *5*, 100088. [CrossRef]
30. Balasingam, B.; Ahmed, M.; Pattipati, K. Battery management systems-challenges and some solutions. *Energies* **2021**, *13*, 11. [CrossRef]
31. Okay, K.; Eray, S.; Eray, A. Development of prototype battery management system for PV system. *Renew. Energy* **2022**, *181*, 1294–1304. [CrossRef]
32. Lipu, M.H.; Hannan, M.A.; Karim, T.; Hussain, A.; Saad, M.; Miah, M.; Mahlia, I. Intelligent algorithms and control strategies for battery management system in electric vehicles: Progress, challenges and future outlook. *J. Clean. Prod.* **2021**, *292*, 126044. [CrossRef]
33. Raoofi, T.; Yildiz, M. Comprehensive review of battery state estimation strategies using machine learning for battery Management Systems of Aircraft Propulsion Batteries. *J. Energy Storage* **2023**, *59*, 106486. [CrossRef]
34. Hamed, M.; El-Tayeb, A.; Moukhtar, I.; el Dein, A.; Abdelhameed, E. A review on recent key technologies of lithium-ion battery thermal management: External cooling systems. *Results Eng.* **2022**, *16*, 100703. [CrossRef]
35. Ebbs-Picken, T.; da Silva, C.; Amon, C. Design optimization methodologies applied to battery thermal management systems: A review. *J. Energy Storage* **2023**, *67*, 107460. [CrossRef]
36. Sezer, H.; Aygun, M.; Mason, J.; Baran, E.; Celik, I. A Computational Model for Sodium Sulfur Battery Analysis. *ECS Trans.* **2015**, *69*, 91. [CrossRef]
37. Vudata, S.; Bhattacharyya, D. Thermal management of a high temperature sodium sulphur battery stack. *Int. J. Heat Mass Transf.* **2021**, *181*, 122025. [CrossRef]
38. Li, H.; Zhang, C.; Sun, B. Optimal design for component capacity of integrated energy system based on the active dispatch mode of multiple energy storages. *Energy* **2021**, *227*, 120522. [CrossRef]
39. Hou, H.; Xu, T.; Wu, X.; Wang, H.; Tang, A.; Chen, Y. Optimal capacity configuration of the wind-photovoltaic-storage hybrid power system based on gravity energy storage system. *Appl. Energy.* **2020**, *271*, 115052. [CrossRef]
40. Panuschka, S.; Hofmann, R. Impact of thermal storage capacity, electricity and emission certificate costs on the optimal operation of an industrial energy system. *Energy Convers. Manag.* **2019**, *185*, 622–635. [CrossRef]
41. Chen, C.; Duan, S. Optimal allocation of distributed generation and energy storage system in microgrids. *IET Renew. Power Gener.* **2014**, *8*, 581–589. [CrossRef]
42. Mostafa, M.H.; Aleem, A. Optimal Allocation of Energy Storage System for Improving Performance of Microgrid Using Symbiotic Organisms Search. In Proceedings of the 2018 Twentieth International Middle East Power Systems Conference (MEPCON), Cairo, Egypt, 18–20 December 2018; pp. 474–479.
43. Qiu, J.; Zhao, J.; Zheng, Y.; Dong, Z.; Dong, Z.Y. Optimal allocation of BESS and MT in a microgrid. *IET Gener. Transm. Distrib.* **2018**, *12*, 1988–1997. [CrossRef]
44. Tripathy, B.K.; Maddikunta, P.K.R.; Pham, Q.-V.; Gadekallu, T.R.; Dev, K.; Pandya, S.; ElHalawany, B.M. Harris Hawk Optimization: A Survey on Variants and Applications. *Comput. Intell. Neurosci.* **2022**, *2022*, 2218594. [CrossRef] [PubMed]
45. Alabool, H.M.; Alarabiat, D.; Abualigah, L.; Heidari, A.A. Harris hawks optimization: A comprehensive review of recent variants and applications. *Neural Comput. Appl.* **2021**, *33*, 8939–8980. [CrossRef]
46. Kim, S.; Kim, J.; Jin, Y.; Yoon, Y. Optimal Bidding Strategy for Renewable Microgrid with Active Network Management. *Energies* **2016**, *9*, 48. [CrossRef]
47. Arif, S.; Rabbi, A.E.; Ahmed, S.U.; Hossain Lipu, M.S.; Jamal, T.; Aziz, T.; Sarker, M.R.; Riaz, A.; Alharbi, T.; Hussain, M.M. Enhancement of Solar PV Hosting Capacity in a Remote Industrial Microgrid: A Methodical Techno-Economic Approach. *Sustainability* **2022**, *14*, 8921. [CrossRef]
48. Koirala, A.; Van Acker, T.; D'hulst, R.; Van Hertem, D. Hosting capacity of photovoltaic systems in low voltage distribution systems: A benchmark of deterministic and stochastic approaches. *Renew. Sustain. Energy Rev.* **2022**, *155*, 111899. [CrossRef]
49. Yuan, J.; Weng, Y.; Tan, C.-W. Determining maximum hosting capacity for PV systems in distribution grids. *Int. J. Electr. Power Energy Syst.* **2022**, *135*, 107342. [CrossRef]
50. Hazır, Ö.; Ulusoy, G. A classification and review of approaches and methods for modeling uncertainty in projects. *Int. J. Prod. Econ.* **2020**, *223*, 107522. [CrossRef]
51. Zhao, Z.; Zhao, J.; Song, K.; Hussain, A.; Du, Q.; Dong, Y.; Liu, J.; Yang, X. Joint DBN and Fuzzy C-Means unsupervised deep clustering for lung cancer patient stratification. *Eng. Appl. Artif. Intell.* **2020**, *91*, 103571. [CrossRef]

52. Heidary, H.; El-Kharouf, A.; Wilckens, R.; Bozorgmehri, S.; Salimi, M.; Golmohammad, M. Life cycle assessment of solid oxide fuel cell vehicles in a natural gas producing country; comparison with proton electrolyte fuel cell, battery and gasoline vehicles. *Sustain. Energy Technol. Assess.* **2023**, *59*, 103396. [CrossRef]
53. Heidari, A.A.; Mirjalili, S.; Faris, H.; Aljarah, I.; Mafarja, M.; Chen, H. Harris hawks optimization: Algorithm and applications. *Futur. Gener. Comput. Syst.* **2019**, *97*, 849–872. [CrossRef]
54. Almotairi, S.; Badr, E.; Abdul Salam, M.; Dawood, A. Three Chaotic Strategies for Enhancing the Self-Adaptive Harris Hawk Optimization Algorithm for Global Optimization. *Mathematics* **2023**, *11*, 4181. [CrossRef]
55. Shahbazbegian, V.; Dehghani, F.; Shafiyi, M.A.; Shafie-khah, M.; Laaksonen, H.; Ameli, H. Techno-economic assessment of energy storage systems in multi-energy microgrids utilizing decomposition methodology. *Energy* **2023**, *283*, 128430. [CrossRef]
56. Alqarni, M. Sodium sulfur batteries allocation in high renewable penetration microgrids using coronavirus herd immunity optimization. *Ain Shams Eng. J.* **2022**, *13*, 101590. [CrossRef]
57. Tercan, S.M.; Demirci, A.; Gokalp, E.; Cali, U. Maximizing self-consumption rates and power quality towards two-stage evaluation for solar energy and shared energy storage empowered microgrids. *J. Energy Storage* **2022**, *51*, 104561. [CrossRef]
58. Wei, W.; Ye, L.; Fang, Y.; Wang, Y.; Chen, X.; Li, Z. Optimal Allocation of Energy Storage Capacity in Microgrids Considering the Uncertainty of Renewable Energy Generation. *Sustainability* **2023**, *15*, 9544. [CrossRef]
59. Gong, Q.; Fang, J.; Qiao, H.; Liu, D.; Tan, S.; Zhang, H.; He, H. Optimal Allocation of Energy Storage System Considering Price-Based Demand Response and Dynamic Characteristics of VRB in Wind-PV-ES Hybrid Microgrid. *Processes* **2019**, *7*, 483. [CrossRef]
60. Zhao, H.; Xu, J.; Xu, K.; Sun, J.; Wang, Y. Optimal Allocation Method of Source and Storage Capacity of PV-Hydrogen Zero Carbon Emission Microgrid Considering the Usage Cost of Energy Storage Equipment. *Energies* **2022**, *15*, 4916. [CrossRef]
61. Zhong, X.; Sun, X.; Wu, Y. A Capacity Optimization Method for a Hybrid Energy Storage Microgrid System Based on an Augmented ε- Constraint Method. *Energies* **2022**, *15*, 7593. [CrossRef]
62. Kreishan, M.Z.; Zobaa, A.F. Scenario-Based Uncertainty Modeling for Power Management in Islanded Microgrid Using the Mixed-Integer Distributed Ant Colony Optimization. *Energies* **2023**, *16*, 4257. [CrossRef]
63. Battula, A.R.; Vuddanti, S.; Salkuti, S.R. A Day Ahead Demand Schedule Strategy for Optimal Operation of Microgrid with Uncertainty. *Smart Cities* **2023**, *6*, 491–509. [CrossRef]